Technische Universität München
Fakultät für Physik

Abschlussarbeit im Bachelorstudiengang Physik

Optical Module Design and Time Synchronization for the Pacific Ocean Neutrino Experiment

Lea Ginzkey

June 26, 2023

Supervisor: Prof. E. Resconi
Second Examiner: Prof. G. Zanderighi
Advisors: Dr. rer. nat. Michael Böhmer, M.Sc. Christian Spannfellner

Acknowledgments

First, I would like to thank my supervising professor Elisa Resconi for providing these interesting topics for my bachelor thesis and granting me the opportunity to participate in the P-ONE collaboration meeting in Krakow. This experience was truly exceptional, and I am very grateful for the chance to be a part of it. Additionally, I would like to thank her for encouraging me to speak at the Deutsche Physikalische Gesellschaft conference 2023 in Dresden.
Furthermore, I want to thank my advisors, Dr. rer. nat. Michael Böhmer and M.Sc. Christian Spannfellner, for their invaluable guidance and support. Michael, I truly appreciate Your patience in addressing all my questions and explaining the time synchronization topic. Thanks, Christian, for Your constructive and detailed feedback and for always being there for me.
I would like to extend my thanks to Chiara Bellenghi for introducing the coupling topic and for her insights to give me an easy start in the lab work.
Finally, I want to thank my family and friends for their support, endurance, and love during this entire journey. Special thanks goes to my friend Natalie for her understanding and support, even while we were on our vacation trip through Canada. Thank you all!

Contents

Abstract

The Pacific Ocean Neutrino Experiment (P-ONE) is a proposed neutrino telescope located off the coast of Vancouver Island. Currently, its first detector line (P-ONE-1) is being developed. This thesis covers two main aspects of the developments for P-ONE-1: the assembly of the optical module and the time synchronization concept. After a brief introduction to Astroparticle Physics and the P-ONE telescope, the integration process of photo-multiplier tubes (PMTs) into the optical module is presented, including the purposes and challenges of the gel pad integration. The feasibility, error reduction, modularity, and mass production suitability were investigated through the construction of prototype optical module hemispheres. I developed a manual for integrating the PMTs into the hemisphere and found that the coupling using 7 g of degassed gel works best to establish an interface between the gel pad and glass of the hemisphere. Using a syringe for pouring the gel is the easiest and fastest option.
The second part of this thesis delves into the communication within the P-ONE detector focusing on timing synchronization which is a crucial part of event analysis and neutrino origin determination. For synchronization, it is of great importance to know the timing delays between each part of the P-ONE detector. Therefore, the delay of different fiber lengths was measured with a special implementation of Gigabit Ethernet (GbE). This thesis discusses the measuring method within a field programmable gate array (FPGA) and its challenges. The delay measurement results within the FPGA are successfully verified by comparing them to the measurement of an oscilloscope.

Chapter 1

Scientific Introduction

1.1 Introduction to Astroparticle Physics and Multimessenger Astronomy

Astroparticle Physics investigates the nature of cosmic objects and their location. The used methods are similar to those in high-energy particle physics. Looking at astronomical messengers such as cosmic rays, neutrinos, gamma rays or gravitational waves, a more detailed insight into cosmic accelerators can be provided. The approach of combining those different kinds of observations from the same astrophysical event is called multimessenger astronomy [1].
The next paragraphs will present an overview of the named astronomical messengers.

Cosmic Rays Predominantly, cosmic rays are accelerated, high-energy protons or nuclei. Before they interact with the earth's atmosphere they are called primary cosmic rays. When traveling toward Earth, cosmic rays interact with atmospheric nuclei, producing a cascade of secondary particles. The basic mechanism for an air shower induced by a cosmic ray proton p interacting with an atmospheric nucleon N is shown in formula 1.1:

$$p + N \rightarrow \pi^{\pm}, \pi^{0}, K^{\pm}, K^{0}, p, n, ... \tag{1.1}$$

The decay of these pions, kaons, protons, and neutrons can produce air showers of high-energy photons, electrons, positrons, muons, and neutrinos through strong interaction with the particles in the atmosphere. With ground-based detectors, the secondary particles can be measured directly or indirectly. However, determining their origin is nearly impossible because charged cosmic rays get deflected by interstellar and intergalactic magnetic fields on their path through the universe [1].

Neutrinos Though abundant in the universe, neutrinos are very hard to detect. Their cross-section is very low as they interact only weakly, are electrically neutral, and have a small mass. Only one neutrino out of 10^{11} interacts when traveling through Earth [1]. But for this reason, they can travel the universe almost without

being deflected or absorbed. This advantage makes locating neutrino sources easier. As a messenger of the high-energy universe potential sources within our galaxy are supernova remnants, pulsars, and micro-quasars. Extragalactic sources are predicted to be gamma-ray bursts (GRBs) and active galactic nuclei (AGNs) [1].
Neutrinos solely interact through the weak force. According to the standard model of physics, neutrinos are leptons with three different flavors corresponding to their charged lepton counterparts: the electron (e), muon (μ), and tauon (τ). Because neutrinos have a mass the lepton number is not conserved and neutrinos can change their flavor over distance. This is called neutrino oscillation. The flavor and mass eigenstate are not equal and have the following relation:

$$|\nu_l\rangle = \sum_i U_{li} |\nu_i\rangle \, , |\nu_i\rangle = \sum_l U_{li}^* |\nu_l\rangle \tag{1.2}$$

The mass eigenstate $|\nu_i\rangle$ is, therefore, a superposition of the three flavor eigenstates $|\nu_l\rangle$ with $l = e, \mu, \tau$. U is a 3x3 unitary matrix called the Pontecorvo-Maki-Nakagawa-Sakata (PMNS) mixing matrix that connects the mass and flavor eigenstates. Hence a neutrino produced with a certain flavor can be measured with a different flavor after traveling a certain distance [2].

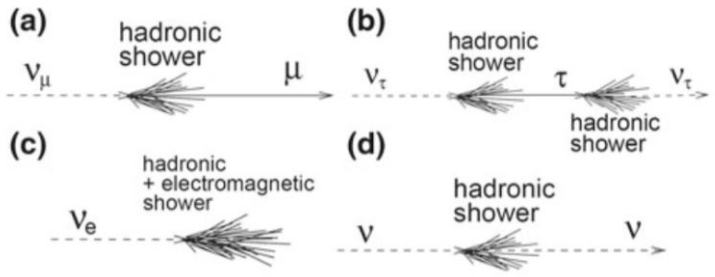

Figure 1.1: Example for event signatures for different neutrino flavors and interactions: **(a)** CC interaction of a muon neutrino (ν_μ) produces a hadronic shower and a muon. **(b)** CC interaction of a tau neutrino (ν_τ) producing a hadronic shower and a τ that decays into a ν_τ and a hadronic shower, generating a double-bang event signature. **(c)** CC interaction of an electron neutrino (ν_e) induces an electromagnetic and hadronic shower at the same time. **(d)** NC interactions produce hadronic showers [1].

When a neutrino interacts with a nucleon N, two reactions are possible: charged current (CC) and neutral current (NC) weak interactions. CC interactions produce charged leptons $l = e, \mu, \tau$ as shown in formula 1.3.

$$\nu_l + N \rightarrow l + X \tag{1.3}$$

NC interactions, depicted in formula 1.4, produce neutrinos, which induce particle showers.

$$\nu_l + N \rightarrow \nu_l + X \tag{1.4}$$

Every interaction type produces hadronic showers but depending on the lepton flavor the CC interactions produce different event signatures. Examples of those possible event signatures are depicted in figure 1.1. In a CC interaction with a muon-neutrino, for example, the generated muon produces a long track before it decays or interacts. Those tracks or showers can be detected through the Cherenkov radiation they emit when traveling through a medium [1]. Cherenkov radiation will be explained in chapter 1.2.

Gamma Rays Gamma rays are high-energy photons produced by cosmic rays propagating through the universe. Those photons emerge from various processes such as bremsstrahlung, synchrotron radiation caused by interstellar and intergalactic magnetic fields, or inverse Compton scattering. When gamma rays collide with matter in the atmosphere, they produce secondary particles. Two detection methods are developed to detect gamma rays. Because the earth's atmosphere is opaque to high-energy photons they either are detected directly by space satellite detectors such as the Fermi-LAT experiment or BeppoSAX who cover a region of MeV to GeV. Or indirectly through the Cherenkov light emitted by secondary particles with ground-based detectors such as MAGIC, HESS, or VERITAS [1].

Gravitational Waves The propagation of distortions in spacetime is called gravitational waves. The first gravitational wave was detected in 2015 which makes them a relatively new member of multimessenger astronomy. They are measured via kilometer-scaled light interferometers. General relativity predicts gravitational waves coming from accelerated objects such as the inspiral and merger of two black holes. Or more generally the inspiral and coalescence of binary systems of compact objects. The core collapse of massive stars could also be the source of gravitational waves but has not yet been detected. Measuring gravitational waves provides information about the binary systems' emitted energy and initial masses. With only one detector it is impossible to locate them but with a network of detectors the origin of the source can be estimated through the difference in their arrival times [3].

1.2 Neutrino Detectors

Before presenting some currently working neutrino telescopes and an introduction to P-ONE, the detection principle of neutrinos will be described.

1.2.1 Detection principles

Because neutrinos have a low cross-section a multi-cubic kilometer detector is necessary for measuring high-energy cosmic neutrinos. The telescope needs to instrument a large volume of a transparent medium such as water or ice to provide a target for neutrinos to interact with and a medium that allows the propagation of Cherenkov photons. Being at a certain depth the medium also acts as a shield for secondary particles induced by cosmic rays and atmospheric neutrinos [1].
The best way to detect neutrinos is through their secondary particles after interaction with the detector medium because direct measurement of neutrinos is technically not realizable. If the speed of those secondary particles exceeds the speed of light in the detector medium, they emit photons called Cherenkov radiation or Cherenkov light. The Cherenkov photons are emitted along a cone with a characteristic angle θ_C.

$$\cos\theta_C = \frac{1}{\beta n} \tag{1.5}$$

The refracting index of the medium is n and β corresponds to the particle speed in units of c. In water, the angle for relativistic particles is $\theta_C \approx 43°$.
A three-dimensional array of multiple photo-multiplier tubes (PMTs) measures the number and arrival time of those Cherenkov photons with high precision. With this information, the flavor, direction, and energy of the detected neutrino can be estimated [1]. For a track-like event usually a muon is detected because the path length of a muon exceeds that of a shower. In that case, it is possible to detect an event that happened outside the detector. With a track event, the direction of the muon and therefore the origin of the neutrino can be reconstructed. A shower event happens in any interaction but needs to arise within the detector to be caught by the PMTs. In this case, the energy of the neutrinos can be reconstructed but the estimation of their direction is unlikely [1].

1.2.2 Current Neutrino Telescopes

BAIKAL-GVD The Baikal Gigaton Volume Detector (BAIKAL-GVD) is operating since 1993 at Lake Baikal in Russia. In winter the ice surface on the lake can be instrumented for the assembly and deployment of the detector without ships or underwater vehicles. Operating at a depth of 1.24 km the lake water suppresses the background. BAIKAL-GVD is located 3.6 km from shore and currently instruments

12 clusters with each 8 strings holding optical modules for Cherenkov light detection. In April 2023, the newly deployed detector lines started operating. It is planned to increase the detector volume to one cubic kilometer by 2027 [1, 4].

KM3NeT KM3NeT is a research infrastructure currently under construction. It hosts a network of three neutrino detectors located in the Mediterranean Sea. The network of KM3NeT neutrino telescopes contains the ARCA telescope for cosmic neutrino detection and the ORCA telescope for studying neutrino properties with neutrinos generated in the earth's atmosphere. Currently, the ORCA detector consists of 18 detection units and ARCA comprises a total of 30 detection units. Once completed KM3NeT will instrument around $3\,\mathrm{km}^3$ cubic kilometers of the Mediterranean Sea [5, 6].

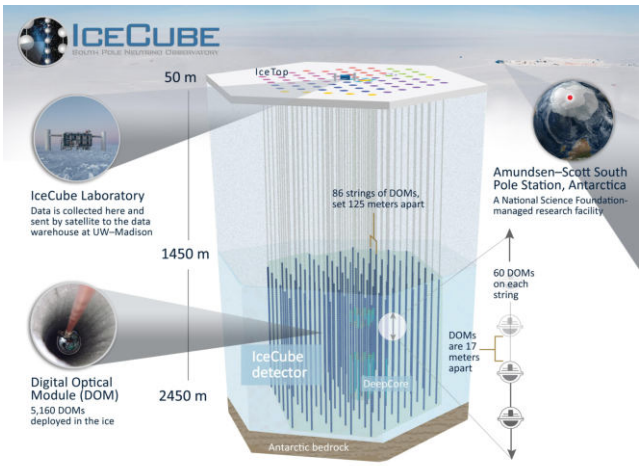

Figure 1.2: The composition of the IceCube Neutrino Observatory. At a depth of 2.5 km, an array of 86 strings with each 60 digital optical modules is deployed in the Antarctic ice. A deep core is designed to measure lower-energy neutrinos [7].

IceCube The IceCube Neutrino Observatory is located at the geographic south pole and was built between 2005 and 2010. Illustration 1.2 shows the structure of the IceCube detector. 86 strings with each 60 digital optical modules (DOMs) are buried beneath the Antarctic ice at a depth of 2.5 km. Every DOM hosts a 10-inch PMT for Cherenkov light detection. IceCube covers the reconstruction of the event direction and energy of high-energy neutrinos as well as low-energy neutrinos in the DeepCore. DeepCore, located within IceCube, is a sub-array of 8 strings with each 60 narrower-spaced DOMs, providing the possibility to study neutrino oscillations by lowering the energy threshold to 10 GeV [1, 7].

1.2.3 The Pacific Ocean Neutrino Experiment

The Pacific Ocean Neutrino Experiment (P-ONE) is a proposed multi-cubic kilometer neutrino telescope located in the northeast Pacific Ocean off the coast of Vancouver Island and aims to detect astrophysical high-energy neutrinos and bioluminescence events. Ocean Networks Canada (ONC) provides the underwater infrastructure for P-ONE at the already existing NEPTUNE observatory. This gives the advantage of an established cable system for data transmission to the shore. The detector will be connected to the Cascadia Basin node shown in figure A.1. This region exhibits favorable characteristics for a multi-cubic kilometer scale detector, including weak currents, a wide and flat area at a suitable depth of 2.6 km, and a stable temperature. P-ONE is planned to complement the coverage of the neutrino sky by the other telescopes (IceCube, Km3NeT, and BAIKAL-GVD). A network of those four telescopes could cover almost the entire sky for high-energy cosmic neutrino observation [8].

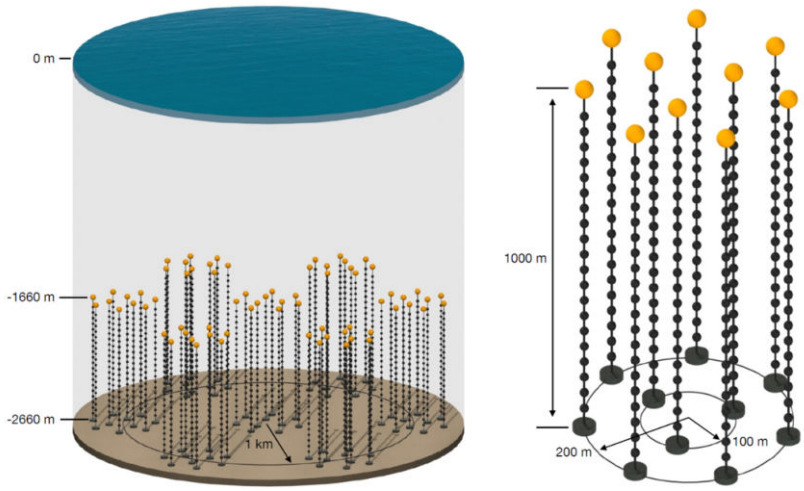

Figure 1.3: Preliminary design concept of the whole P-ONE detector. At a depth of 2.6 km in the ocean, a total of 7 clusters with each 10 detector strings is planned. Every detector line contains 20 optical modules and has a length of 1 km [9].

Figure 1.3 visualizes the detector structure with 70 mooring lines that are organized in 7 clusters. Each detector line contains 20 optical modules of two types: optical modules (P-OMs) and calibration modules (P-CAL). The detector will operate at a depth of 2.6 km where the ocean water shields the detector from cosmic rays and atmospheric neutrinos and at the same time provides a target volume for neutrino interaction [8, 9].

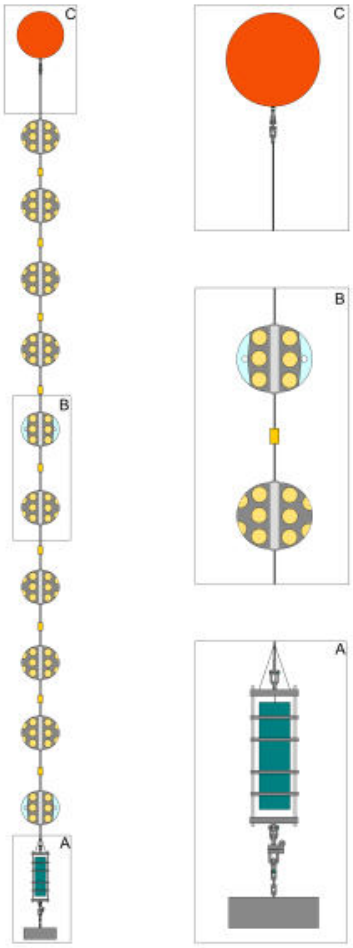

Figure 1.4: Prototype line structure of P-ONE-1 including an anchor, a mini junction box, the optical and calibration modules, and buoy. For illustrative purposes, the picture depicts only 10 modules instead of 20 [8].

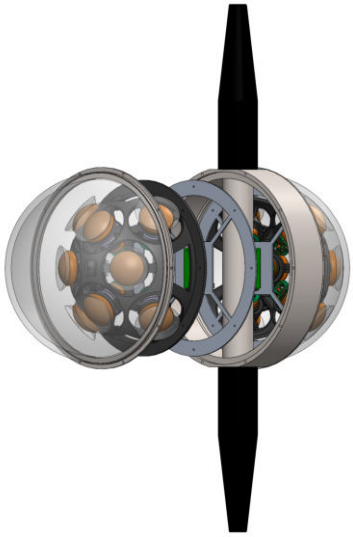

Figure 1.5: Current optical module design: two glass hemispheres held together by a titanium ring. 8 PMTs per hemisphere are placed within the black frame [Graphic kindly provided by Christian Spannfellner].

P-ONE-1 The prototype detector line of P-ONE is called P-ONE-1 and is currently under construction, its structure is depicted by figure 1.4. Although the line will incorporate 20 optical modules the figure only depicts 10 modules for graphical reasons. At the top, a buoy will stretch the 1 km tall line and at the ground, an anchor fixes the line to the seafloor. In between 20 optical modules are mounted, containing about 2-3 calibration modules. A mini junction box (mJB) centralizes

the communication at the bottom of the line. The electrical-optical-mechanical cable penetrates the titanium assembly, passes the optical modules, and terminates in the mJB [8]. The optical modules (P-OMs) aim to detect bioluminescence and Cherenkov light with a multi photo-multiplier tube (mPMT) configuration depicted in figure 1.5. The module consists of two glass hemispheres, each with a radius of 201.9 mm, which are connected to a titanium head ring cylinder. In each hemisphere, eight 3-inch PMTs are placed within a 3D printed frame and securely held in place by a holding structure consisting of a collar, spring, and lock (see figure 2.8) to ensure proper alignment as well as securing the PMTs while also providing some flexibility for vibrations. A gel pad is placed between the glass of the hemisphere and the PMT. These gel pads serve multiple purposes and therefore need special optical properties further discussed in chapter 2.
With the calibration module the optical properties, geometry of the P-ONE sensor arrays, and sedimentation effects can be constantly monitored. For this, a high-intensity nanosecond light flash is emitted and detected by the surrounding P-OMs. This enables the measurement of light attenuation through the analysis of flash intensity [9, 10].
Time synchronization between each part of the detector line will be transmitted through optical fibers [10] and uses Gigabit Ethernet (GbE) as a data transfer protocol. Chapter 3 discusses the timing system of P-ONE more in detail.

Chapter 2

Optical Module

The assembly of the P-OMs is a critical step in the construction of P-ONE and its first detector line P-ONE-1. An important production step is the placement of PMTs in the hemisphere with interposed gel pads. To ensure optimal photon detection the gel pads serve three purposes: with a refraction index similar to glass, they minimize the refraction across the different media around and in the optical module (water, glass, and air), while enhancing the angular acceptance with reflecting gel pad sides. Thirdly, the gel pads help secure the PMTs in their position together with a mounting structure involving a frame. While the design of the P-OM and frame is nearly complete and a procedure for gel pad production is established, integrating the PMTs presents challenges. The following chapter focuses on investigating the integration process, addressing the question of feasibility and error reduction as well as the following requirements: easy PMT removal for maintaining a modular approach and achieving a bubble- and dust-free coupling between PMT and gel pad as well as gel pad and glass. Additionally, the integration process is investigated to be suitable for mass production scenarios. To accomplish this, I constructed two prototype optical module hemispheres. Through iterative integration attempts, I improved the coupling results and developed a guide for the future mounting of P-ONE-1 optical modules.

2.1 Gel Pads

The gel pads are interposed between the PMTs and the glass of the hemisphere and aim to fulfill two key properties. They need to satisfy different optical properties for optimal photon detection and be resistant to stress. During my work on the coupling of those gel pads, some improvements in the design were made, which will be discussed in this section.
Before going more into detail on the gel properties an introduction to the behavior of light in different mediums is necessary, as the Cherenkov photons will traverse water, glass, and gel before they get detected in the PMT.

2.1.1 Overview on Refraction and Reflection

The propagation speed of light in a medium v is lower than the speed of light in vacuum c. The relationship between those two velocities is defined by equation 2.1, where n represents the refractive index, characteristic for different materials.

$$v = \frac{c}{n} \tag{2.1}$$

When light transitions from one medium with refractive index n_1 to another with refractive index n_2 it gets deflected. With Snell's law of refraction (see equation 2.2) the angle of refraction can be estimated. In this equation, α denotes the angle at which the light beam hits the boundary between the two media and β represents the angle of refraction.

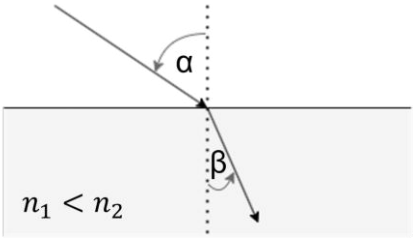

Figure 2.1: Based on Snell's law of refraction this picture shows how the light gets refracted during the transition from one medium 1 to a medium 2 with a bigger index of refraction n_2 (image inspired by [11]).

$$\frac{\sin\alpha}{\sin\beta} = \frac{n_2}{n_1} \tag{2.2}$$

If the refractive index of medium 1 is lower than that of medium 2, the refraction angle β is smaller than the initial angle of incidence. This relationship is illustrated in figure 2.1. When $n_1 > n_2$, the angle of refraction is bigger than α. At a critical angle $\alpha_c = n_2/n_1$, the light does not transmit into medium 2 but instead gets reflected, known as total internal reflection [11].

2.1.2 Properties

The gel used for the gel pads in the optical module requires three optical properties to ensure efficient photon detection. Firstly, the gel needs to be transparent to allow light transmission without significant absorption or scattering for optimal photon detection. Additionally, the gel pad should minimize refraction at its interface with the glass of the hemisphere to prevent photon losses during their propagation toward the PMT. This can be achieved by having a similar refractive index as glass, which reduces the refraction of light at the gel-glass interface, leading to increased photon detections. Moreover, by matching the refractive index, the reconstruction of the photon path becomes easier. Thirdly, we seek to enhance the angular acceptance of the optical module with a gel pad design that enables total internal reflection and redirects the photons toward the PMT. The refractive index of the gel is larger than the refractive index of air, which ensures total internal reflection at a certain angle.

With the inclined sides of the gel pads photons, that would otherwise have passed, get reflected into the PMT, increasing the angular acceptance for photon detection [12].
In addition to the optical properties, the gel pads must also exhibit stress resistance to ensure the stability and performance of the system. Transportation and deployment of the optical module as well as P-ONE-1 will induce shaking and vibrations. The gel pads need to withstand these vibrations, protect and maintain the positioning of the PMTs. For that reason, the used gel is relatively soft and flexible to a certain extent. Moreover, the gel pads need to endure different thermal expansion rates. The ocean water temperature surrounding the module is typically around 2°C [8]. The internal components, including the electronics, generate heat, causing a temperature gradient between the outer layer and the core of the optical module and thus also within the gel pad. Hence the gel pads should be resistant to the resulting thermal stress [12].

2.1.3 Gel Pad Design Changes

The gel pads are designed to match the curved surfaces of both the PMT and hemisphere. To ensure total internal reflection, the sides have a certain angle. The gel pads used in this thesis were produced in three different molds with slightly different features.

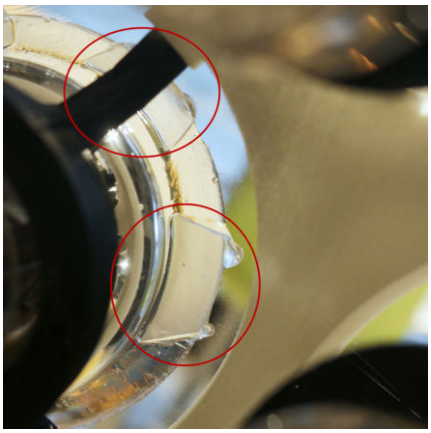

Figure 2.2: Gel pad seen from the inside of the optical module where the opaque marks from the coupling process of the standalone gel pad to the PMT are visible on the surface.

Standalone Gel Pads For the prototype hemisphere, we used standalone gel pads which first had to be attached to the PMTs before integrating the PMT-gel pad assembly into the hemisphere. To achieve this coupling, I applied gel onto the gel pad and gently pressed it onto the previously cleaned PMT. The PMT-gel pad system was either cured with the PMT or the gel pad on top. The excess gel overflowed in every curing scenario but with the PMT on top, it proved easier to remove the gel after curing. Furthermore, this method prevented spilled gel from affecting the surface properties on the sides of the gel pad. To ensure the central placement of the gel pad on the PMT, we employed an alignment tool. However, using the alignment tool presented two draw-

backs: firstly, it detached the gel pad from the PMT, and secondly, it left opaque marks on the sides of the gel pad as illustrated in figure 2.2 affecting their optical properties.
In addition, the coupling to the PMT affects the production speed negatively since the gel requires 24 h to cure at room temperature [13, 14]. Each additional production step involving curing of gel contributes to the overall production time as well as the cleaning of the spilled gel.
At last, the pushing of the gel pad onto the PMT may have caused the surface of the gel pad to become uneven. This could be the reason for some miscarried couplings along with difficulties in estimating the appropriate amount of gel.

Gel Pad Mold including the PMT To facilitate the integration and avoid the problems described above a new mold for the gel pad production was developed. Figure 2.3 illustrates the profile of this mold, which is characterized by the fact that the PMT is integrated into the production process. The PMT couples to the gel pad directly reducing one step in the production line. This decreases the production time, and error proneness and at the same time increases the practicability. This mold was used to produce PMTs with gel pads in the integration of the second hemisphere and it stands as the preferred medium for future production of optical modules intended for P-ONE-1.

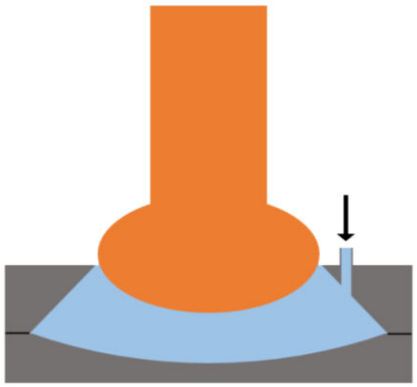

Figure 2.3: Sketch of the gel pad production technique. The gel pad is produced directly on the PMT by integrating the PMT in the mold and pouring the gel in.

Different Gel Pad Radii To determine which gel pad design achieved better couplings, we tested two different radii for the gel pad surface coupling to the hemisphere. One matches the diameter of the hemisphere with $r = 201.9\,\text{mm}$. The other has a smaller diameter than the hemisphere with $r = 190\,\text{mm}$. The smaller diameter gel pad was introduced to enhance the coupling of the gel pad to the hemisphere and minimize the occurrence of bubbles. The idea behind this approach was to ensure that the gel pad, with the diameter matching the radius of the hemisphere, would couple to the glass before any air enclosures could form during the curing process. By employing a smaller radius, the gel could have sufficient space to flow out. Thus, it would reduce

the likelihood of forming trapped bubbles and promote effective coupling between the gel pad and the glass surface. Apart from the difference in the amount of gel required for a good coupling (the gel pad with the smaller diameter needed approximately 8 g of gel and the bigger diameter gel pad required 7 g) we did not observe a significant difference in the quality of the coupling, so we decided to use the gel pad design matching the diameter of the hemisphere.
With this progress, we can now proceed to discuss the optical coupling of the PMT-gel pad assembly to the glass of the hemisphere.

2.2 Optical Coupling to the Hemisphere

The first coupling attempt involved only pressing the gel pad with the PMT on the glass of the hemisphere. This method resulted in an incomplete coupling, possibly due to an uneven glass surface that prevents the gel pad from filling all gaps. Hence air got trapped between the glass and the gel pad. Additionally, the pressure of the spring might have deformed the surface of the gel pad, causing the edges to slightly go up. This can be observed in the integration shown in figure 2.4, where only the middle of the gel pad couples to the glass and the sides of the gel pad do not. Based on this experience we decided to introduce gel between the gel pad and the hemisphere.

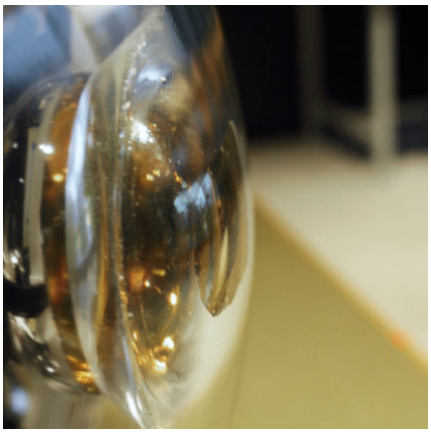

Figure 2.4: Gel pad coupling without interface gel seen from the outside of the hemisphere. Only the middle of the gel pad couples well with the glass.

The overall integration procedure started with a thorough cleaning of the glass. Then, the hemisphere was aligned to ensure the PMT can be placed perpendicular to the glass surface. Next, the gel was mixed according to the specified mixing ratio and degassed in a vacuum chamber. For coupling, varying amounts of gel were applied to the glass surface of the hemisphere, as shown in figure 2.5. The PMT was secured either using an alignment tool (figure 2.7), where the gravitational force presses the PMT down, or a holding structure with a spring putting additional pressure on the construction (figure 2.8). Both structures ensure proper alignment of the PMT. Results for those two approaches are discussed in paragraph 2.2, covering the curing process and overflow of gel. After curing for 24 h, the interface gel merges with the gel pad, resulting in complete coupling to

the glass of the hemisphere. If not applied earlier, the holding structure was locked into place after curing. In this manner, I integrated two hemispheres with each eight PMTs.
The next paragraphs compile and classify the results to elaborate a guide for the optimal integration method using the current gel pad design.

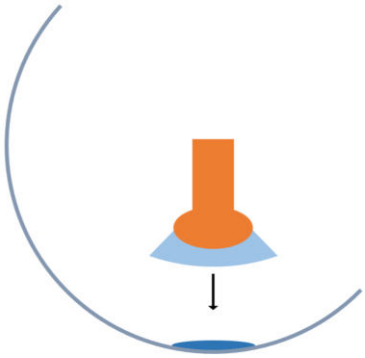

Figure 2.5: Integration method: pour a blob of gel onto the hemisphere and place the PMT with the gel pad on top.

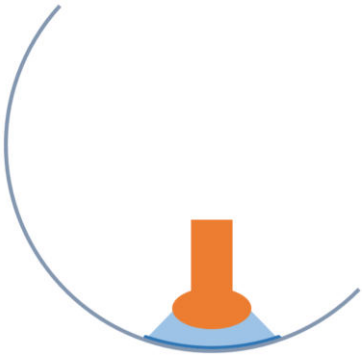

Figure 2.6: After curing, a little overflow of gel remains on the glass. And the gel pad coalesces with the interface gel.

Figure 2.7: The alignment tool holds the PMT in place without putting pressure on it. This makes sure the PMT and gel pad are perfectly aligned in the hemisphere.

Figure 2.8: The holding structure holds the PMT in place and is applied after the gel is cured. It consists of a lock that is seized into the white frame, a spring, and a collar, all placed around the neck of the PMT.

Gel Types For the coupling of the PMT-gel pad construction onto the glass of the hemisphere I tested two different types of gel which are already approved for the gel pad production and therefore fulfill the required properties (see section 2.1.2) [12]. The main gel pad component is Silgel 612 from Wacker, a two-component silicone gel with a mixing ratio of A:B = 1.5:1 [14]. The rather tacky texture of Silgel 612 makes the removal of a coupled PMT challenging. We had to scrape off the gel pad, resulting in significant damage to the gel pad, as shown in figure 2.9. Thus, some gel residues were left on the glass which required time-consuming and extensive cleaning. The second gel type, Wacker Elastosil RT 601, is used as a coating gel for the gel pads and is less tacky, facilitating easy removal of the gel pad from the mold. The mixing ratio for this gel is A:B = 9:1 [13]. Coupling with this gel makes the removal process much easier. We only needed to lift the edge of the gel pad and, by turning and levering, the PMT including the gel pad and interface gel came off completely (see figure 2.10). Consequently, no gel residues were left on the glass which makes cleaning more feasible. Both gels require 24 h curing at room temperature [13, 14] and there is no difference in the quality of the coupling for both gel variants. Hence, considering the practicability of PMT replacement, using coating gel as interface gel is the preferable option.

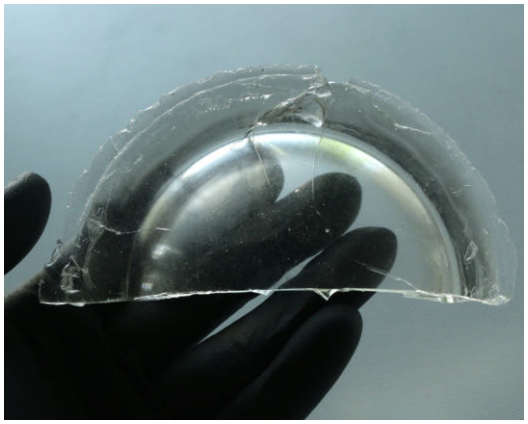

Figure 2.9: Picture of a gel pad after removal. As interface gel Wacker Silgel 612 was used, resulting in a stronger adhesion to the glass and damage to the pad after separation. This left some gel remnants on the glass.

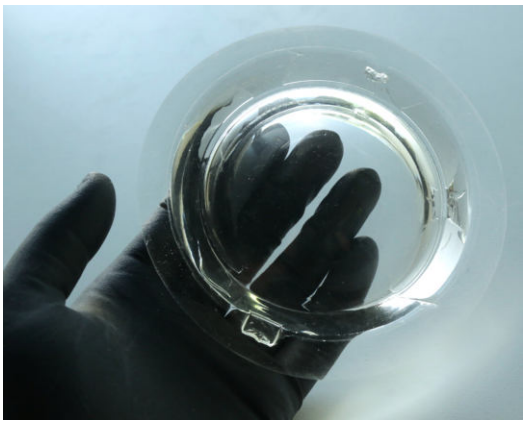

Figure 2.10: Picture of a gel pad after removal. This gel pad was integrated with Wacker Elastosil RT 601 which doesn't adhere as strongly to the glass as Silgel and separated completely. No gel residuals were left on the glass surface after removal.

Figure 2.11: The interface gel in this integration at first flowed out enough but came back during the curing process, leaving the edges of the gel pad with not enough gel for a complete coupling.

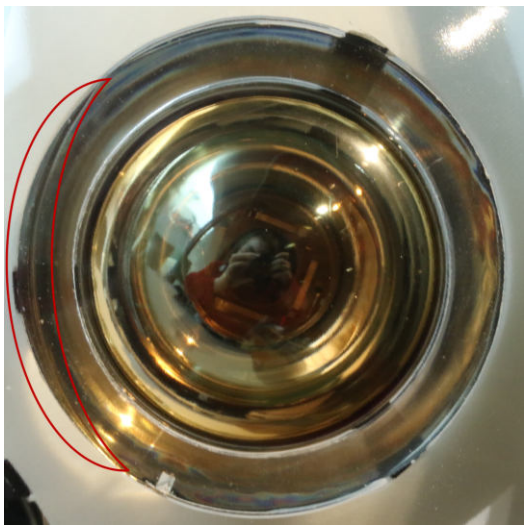

Figure 2.12: Here we used not enough gel for a throughout coupling as a little gap between the gel pad and glass is visible on the left side.

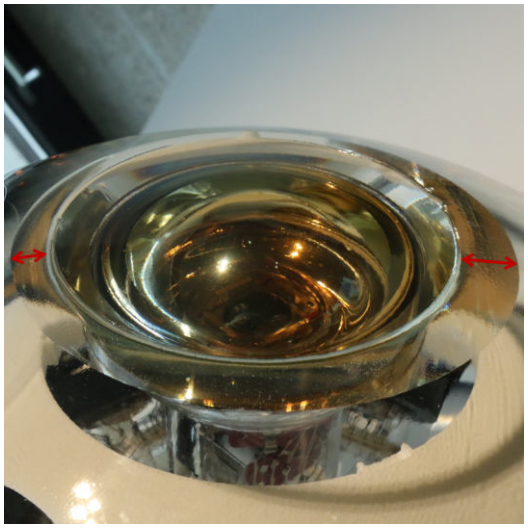

Figure 2.13: In this picture the gel overflow is too large, leaving a big ring of interface gel on the hemisphere. The gel did not flow out evenly, leaving a different brim thickness.

Figure 2.14: This gel pad is coupled fully to the hemisphere with only a little amount of interface gel flowing out on the sides. However, the overflow is not even: on the top right edge of the gel pad no overflowing gel is visible.

Curing and Gel Overflow Figure 2.11 shows a coupling where the gel overflowed in its liquid form. Nonetheless, after curing, a gap formed between the gel pad and hemisphere, resulting in an incomplete coupling. It appears that the overflowed gel retreated during the curing process, leaving gel residues beyond the gel pad and the visible cavity. In cases like this, we let the gel cure with the holding structure in place, which applies additional pressure to the PMT and gel pad, and we tried to wipe away the excess gel as soon as it flowed out. Hence the incomplete coupling could have occurred because the pressure caused the gel pad to slightly lift the edges, increasing the volume between the gel pad and hemisphere, preventing a throughout coupling. Another reason could be that cleaning the excess gel immediately left us with an inadequate amount of gel to flow back between the gel pad and the glass. Additionally, the previously addressed problem of an irregular surface resulting from the coupling of the standalone gel pads to the PMT could contribute to failed couplings like this. For these reasons, we decided to let the gel cure without cleaning, started using the alignment tool for curing, and applied the spring afterwards. Without the pressure and the more even gel pads with the mold producing the gel pad directly on the PMT, this kind of coupling no longer occurred. Furthermore, the packed structure within the hemisphere made it difficult to sufficiently clean the overflowing gel. Overall, we found that the integration produces cleaner results when the overflow gel is left to cure, leaving a gel ring around the gel pad. Simulations are currently ongoing to determine the effect of this brim on the photon collection.

Gel Pouring and Amount of Interface Gel Initially, the plastic cup used for preparing the gel was also used for pouring it onto the glass. To estimate the required amount of gel, the cup with gel was weighed before and after pouring. Usually, I had to pour multiple times until I approximated the desired amount of gel, making the process time-consuming. Supposably, the amount of gel often was inaccurate.
To address these challenges, I attempted to use a syringe for measuring and pouring the interface gel. However, this posed two new challenges: drawing the gel up without creating air bubbles and cleaning the syringe for reuse. As shown in figure 2.15, the first trial with a syringe produced some small bubbles at the edge of the gel pad. They can be avoided by drawing up the gel slowly and carefully. Allowing the syringe to rest with the tip up for a few minutes causes the bubbles to rise, after which excess air can be pressed out, leaving only pure gel behind. If any air bubbles remain on the gel surface after injection on the glass, they can be easily popped with the end of a spatula. Cleaning the syringe is still time-consuming and fiddly but considering mass production with multiple integrations at a time, this can be put into perspective.
Determining the correct amount of interface gel became a crucial part of the integration process once we decided to leave the gel brim around the gel pad. Fine-tuning

the amount of gel was necessary to achieve a complete coupling to the glass of the hemisphere while ensuring that the gel ring does not exceed the edges of the gel pad excessively, as shown in figure 2.13. With every change in the gel pad design the fine-tuning began anew. An example of coupling with insufficient gel can be seen in figure 2.12 where 6 g of gel was used for the current gel pad design. Adding 1 g of gel resulted in complete coupling with a minimal gel ring, as depicted in figure 2.14. For the current gel pad design using 7 g of gel results in a thorough coupling while producing only a small gel brim. The gel is poured with the help of a syringe which proved to be an acceptable solution for measuring the amount of interface gel.

Alignment of the Hemisphere The hemisphere is tilted and aligned with a holding device, as depicted in A.3. Despite additionally using a bubble level for alignment, it was challenging to even out the hemisphere for the PMT to go perpendicular to the surface. This challenge in the correct placement causes the gel to not expand equally to each side of the gel pad as shown in pictures 2.13 and 2.14. This alignment issue could be related to the alignment of the table or slight irregularities of the holding device as well as the placement of the bubble level within the curved frame. It is worth investigating if using other equipment for aligning the hemisphere improves the results.

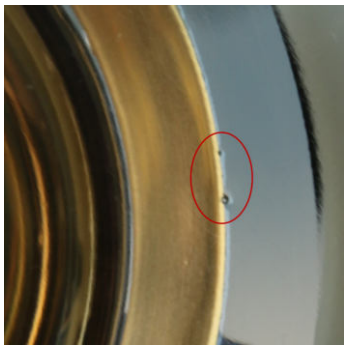

Figure 2.15: Even after degassing the interface gel exhibits small bubbles at the edge of the gel pad.

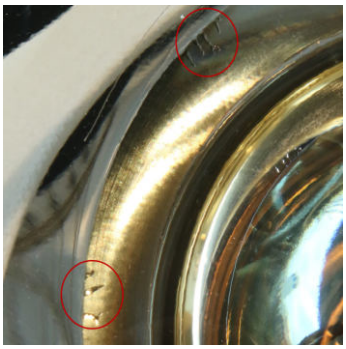

Figure 2.16: When using too much gel sometimes tree structures form on the surface of the gel pad.

Figure 2.17: Here the gel flowed out strangely and creates this folded structure at the edge of the gel pad but couples fully nonetheless.

Other Observations In some coupling approaches, small tree-like structures formed on the sides of the gel pad after curing, as depicted in picture 2.16. The formation of these structures is not yet completely understood and requires further invest-

igation. We currently presume they could originate from dust particles, dirt, or grease. Micro scratches from the unpolished mold causing the gel to flow up through capillary action or the conveyance of the gel pad during the integration could also be conceivable reasons.
When using less gel, deformed gel borders sometimes appeared, as shown in figure 2.17. This may be attributed to the surface tension of the gel and the imperfect alignment of the hemisphere, causing the gel to flow out and cure unevenly. Grease, dirt, or dust could also cause a strain on the overflowing gel. Further investigations are needed to understand the origin of these deformed borders.

In conclusion, I found that the integration is cleaner and more efficient when using a syringe to pour a droplet of 7 g gel onto the hemisphere and then placing the PMT with the gel pad on top. This method is the fastest and ensures a complete coupling of the gel pad to the glass. Leaving a gel brim after curing yields the most satisfactory coupling results. Further investigations are necessary to improve the alignment of the hemisphere and understand the formations of tree-like structures and deformed gel rings.

2.3 Manual for the Integration of the PMTs into the Hemisphere

With the investigations from above I worked out a guide on how to integrate a PMT with a gel pad into the hemisphere properly. Note that in every step of working on the optical module wearing gloves is mandatory to keep the environment clean. Working in a clean room is recommended to avoid trapping dirt and dust particles, which would disturb the optical properties.

1. Gel Preparation
    a) Use Wacker Elastosil RT 601 and pour 13.5 g of component A and 1.5 g of component B into a clean cup (this makes 15 g of gel with a mixing ratio of A:B = 9:1).
    b) Mix it with a spoon for about 2 min.
    c) Degas the gel mixture for about 5 min in a vacuum chamber while stirring it with an automatic stirring device (figure A.4).
2. Preparation of the Hemisphere
    a) Clean the surface with isopropanol right where the gel pad will be placed.
    b) Align the hemisphere ideally with a spirit level so that the PMT can be placed perpendicular to the ground.

3. Integration
    a) Draw up the syringe slowly and carefully with a little more than 7 g (figure A.5).
    b) Let it rest upside down until the drawn-up air raises and no bubbles are visible in the gel.
    c) Press the excess air out of the syringe.
    d) Inject 7 g gel onto the glass surface slowly to prevent inducing any bubbles (figure A.6).
    e) Place the PMT with gel pad into the alignment device and hold the PMT upside down on its neck.
    f) Carefully insert the PMT and gel pad with the holding structure in the frame and lower the PMT until it touches the gel (graphics 2.5 and 2.6).
4. Curing and Applying the Holding Structure
    a) Let it cure for 24 h.
    b) Remove the alignment tool and place the collar, spring, and lock of the holding structure on the neck of the PMT (figure 2.8).
    c) Lock it in place by pushing the lock down and turning it until it is placed under the extensions in the frame.

Chapter 3

Timing and Sychronization

The previous chapter described the optical module of P-ONE, with focus on the optical coupling of the PMTs. Now, the communication within the P-ONE detector will be discussed. Once the PMT detects photons, the waveform signal is stored within the optical module and gets a label with timing information. When a data set is requested, it is sent to the mJB at the bottom of each detector line for further processing. The location and timing information of the detected signals enables recreating the neutrino events and is therefore a crucial part of the event analysis. P-ONE thus needs to synchronize its detector parts to provide this information with nanoseconds accuracy. The clock gets transferred from the mJB to all P-OMs and back through GbE. Because of the different fiber lengths between the mJB to each optical module, the clock operates with a phase shift. This is called a syntonous system. Knowing all phase differences in the detector provides the information to synchronize the signals and reconstruct the timing of the measured photon hits. This chapter introduces some digital technology basics and gives an overview of the used technologies before presenting the measurement method and the results of the first delay measurements.

3.1 Background and Theory

3.1.1 Introduction to Digital Technology and Data Transmission

Processing data in digital systems works with combinatorial and sequential logic. Combinatorial circuits use so-called logic gates that process two or more data inputs into one data output using logic operators. An AND gate for example only generates a 1-output if input A and B are 1, otherwise, it generates 0, as shown in table 3.1. Sequential circuits can memorize data through Flip Flops (FFs). Every FF uses a clock operating with a constant frequency to save current or previous inputs. They are installed as edge detectors, counters, or controls. A D-Flip Flop (D-FF) for example has a data input, a clock, and a data output. The D-FF is active with either the rising or falling edge of the clock, meaning it samples the incoming data and saves it in the output data as shown in the clock cycle illustration in figure 3.1.

To create a decent signal, the input data must be stable just before and after a clock edge, this is called setup and hold-up time [15].

gate name	output for AB=			
	11	**01**	**10**	**00**
AND	1	0	0	0
OR	1	1	1	0
XOR	0	1	1	0

Table 3.1: Logic table showing the output for three examples of logic gates with two binary input parameters [15].

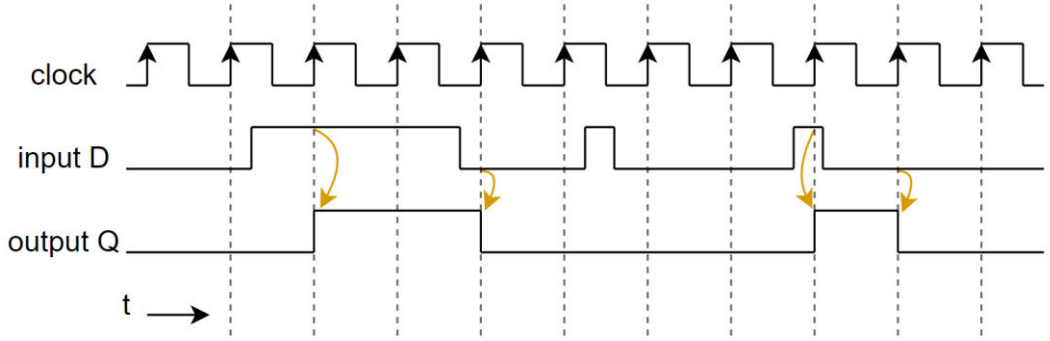

Figure 3.1: Time response of a D-Flip Flop which is active with the rising edge of the clock (image inspired by [15]).

For data transmission in P-ONE as well as P-ONE-1 GbE was chosen. GbE is a protocol for data transmission consisting of several functional layers. We are operating on layer 1. It is responsible for the data link, maintaining the connection, and thus keeping the system ready for data transmissions. For that, it uses either data signals or administrative signals called K-Characters. With the help of a special coding scheme (e. g. comma characters), the beginning and ending of a transmission are set. In GbE usually, the transmitted signals carry 16-bit information namely two 8-bit 'words' [16]. For P-ONE-1 we implemented an 8b/10b encoding which translates an 8-bit word to a 10-bit word [17].
In our setup, we are using two TRB3sc boards [18] with each a Field Programmable Gate Array (FPGA) shown in picture 3.2. An FPGA can be explained as programmable logic with fixed hardware consisting of logic blocks as well as input and output blocks. An example of these input and output blocks is a Seri-

alizer/Deserializer (SerDes) which converts parallel data into a serial data stream for transmission and converts the received serial data into a parallel data stream. The logic blocks can be individually programmed by the user and a central clock with a frequency of 125 MHz ($T = 8$ ns) is ideally providing a synchronous signal for the whole FPGA. In reality, the clock signal has a slight time shift for distant logic blocks due to time delays in the wires [15]. Within the SerDes of the used FPGA, a special module can be programmed for word alignment operations. Here, the comma character is used to perform the 10-bit word alignment. This means that it can be determined and specified at which position of the word a signal is read out. Knowing the word alignment position is crucial for delay measurement as each word alignment position changes the delay [19]. A word consists of 10 bits after 8b/10b encoding, so each word position changes the delay by 8 ns/10 =800 ps (whereat 8 ns derive from the periodic time of the central clock).

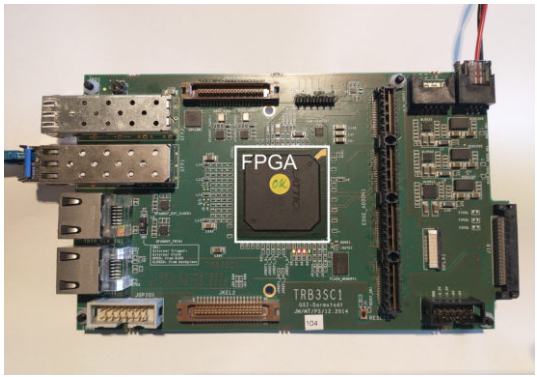

Figure 3.2: The used TRB3sc board with the FPGA right at the center. The signal out and input are on the left side where the fiber is connected to the board. The red and black cable provides power to the board.

3.1.2 Concept of Timing and Synchronization using the Example of White Rabbit

The delay measurements discussed in this thesis are part of a timing and synchronization system called BlackCat and are used for the synchronization of the P-ONE prototype line. BlackCat is a synchronization system already proven and tested for another communication protocol called TRBnet. TRBnet is used for example in the HADES experiment [18, 20] as well as the pathfinder experiments for P-ONE: STRAW-a and STRAW-b. However, for P-ONE we use GbE for data transmissions because it is a well-established communication protocol. The concept of BlackCat was adopted one to one to GbE. In the following paragraphs, I use White Rabbit as an example to explain the concept of timing systems. Then the differences to BlackCat are pointed out.
White Rabbit (WR) is an evolution of the General Machine Timing system at CERN and was started in 2008. WR allows the synchronization of many different processes

at CERN networks, needs careful calibration and uses GbE as communication protocol. For synchronization three different aspects work together: Precise Time Protocol (PTP), layer-1 syntonization, and precise phase measurement. PTP evaluates the link delay between two nodes via time stamps and with that provides 1 μs accuracy. To achieve an accuracy of sub ns with layer-1 syntonization the time stamp problem gets transferred to a delay measurement problem with a master providing a clock to all followers in the system. As the phase shift of the layer-1 distribution of the clock is directly linked to the link delay in PTP, the phase shift is evaluated with Precise Phase Measurement for which they use digital DMTD, which will be explained later in section 3.3, and makes it possible to measure the phase with greater accuracy than the clock. With those three approaches working together, WR estimates the link delay and uses this information for synchronizing the follower clocks with a special switch and phase-locked loops (PLLs). Thus after calibration, the whole system works simultaneously [21].
BlackCat works similarly to the described method of White Rabbit but does not use the WR switch and PLLs for synchronizing the detector parts because those components are not suitable for use in the deep sea as they require ventilation. Additionally, by only using TRB3sc boards with FPGAs the synchronization brings more software effort but is easier to develop and much cheaper. Consequently, instead of synchronizing each detector part, we opt for syntonization, wherein we operate on layer-1 of GbE, distributing a central clock through the entire detector. By employing precise phase measurement techniques, described in section 3.3, we estimate the round trip delay of a signal pulse for each individual path within the detector.

3.2 Experimental Setup

In P-ONE-1, each optical module is connected to the mJB using point-to-point optical fibers. The central clock and the synchronization signal are distributed by the FPGA in the mJB to all optical modules and back to the mJB. To replicate this data stream, our experimental setup (shown in picture 3.3) measures the round-trip delay for different fiber lengths. For this purpose, we use two TRB3sc boards, each equipped with an FPGA connected through optical fibers of varying lengths. One FPGA provides the clock for the system. The clock signal, along with the pulse signal, is transmitted (TX) from the first FPGA through the fiber. The second FPGA receives (RX) and processes the clock and pulse signals before transmitting them back. The delay measurement takes place within the first FPGA using the transmitted and received signal. Moreover, an interposed oscilloscope measures the delay to provide a reference value. In the following, the stated measurement is referred to as the ‘normal round trip’ delay measurement (figure 3.4).

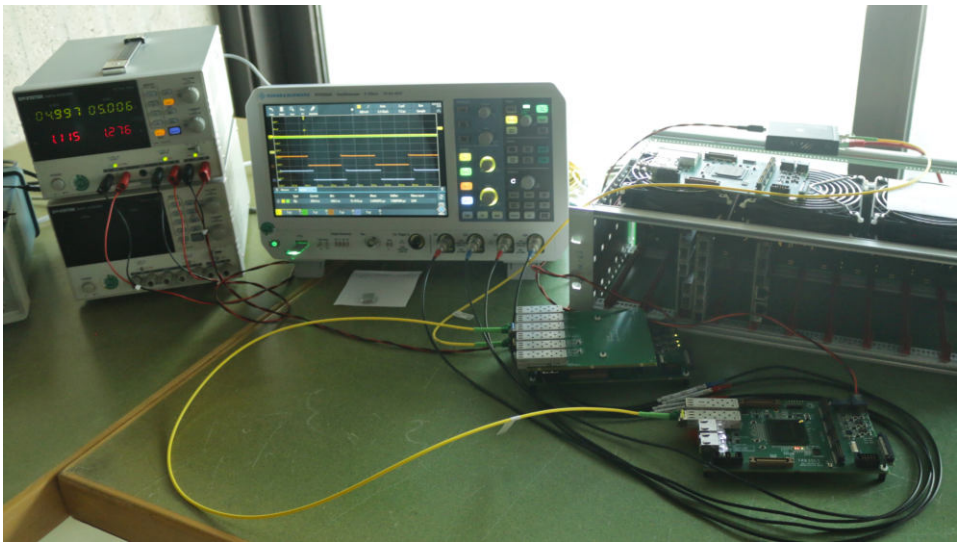

Figure 3.3: Setup for the delay measurement. The TRB3sc board on the left side sends out the pulse and measures the phase difference. The yellow fiber connects the two TRB3sc boards. An oscilloscope taps the two signals and visualizes the delay measurement and at the same time provides a reference value.

We conducted two additional measurements: the remote loopback and local loopback delay measurement, as illustrated in figure 3.5 and 3.6. The remote loopback determines the signal delay without involving data processing within the second FPGA. Instead, a copy of the received signal is directly sent back through the transmitter of the SerDes in the second FPGA. In the local loopback measurement, solely the delay within the first FPGA is determined, where the pulse is transmitted through the SerDes. A copy of the outgoing signal is transferred to the receiver and sent back to the delay measurement immediately.
The next section discusses the details of how the delay measurement within the FPGA is performed.

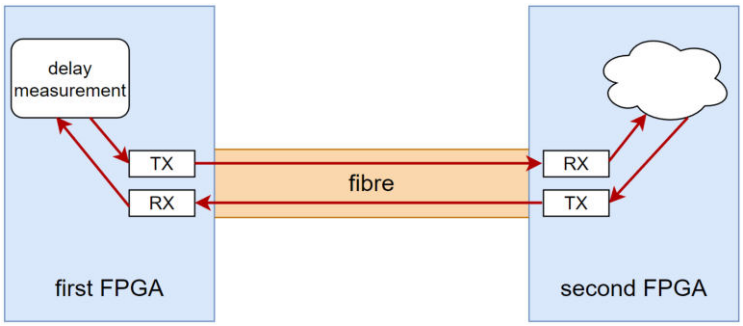

Figure 3.4: Normal round trip: the signal from the first FPGA leaves the transmitter (TX), travels through the fiber, and reaches the receiver (RX) of the second FPGA. The signal gets processed in the fabric of the FPGA and is sent back. The phase difference of the transmitted and received signal is measured within the first FPGA.

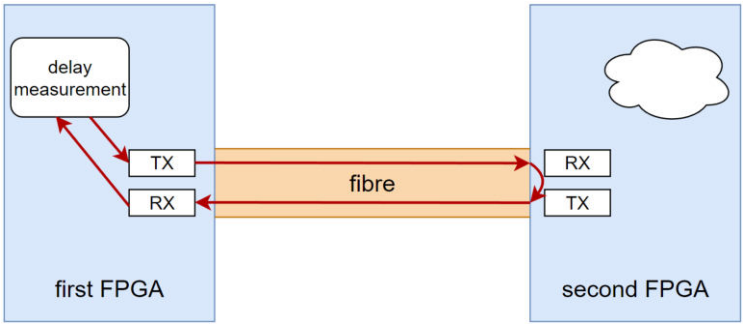

Figure 3.5: Remote loopback: the signal from the first FPGA leaves the transmitter, travels through the fiber, and reaches the analog receiver of the second FPGA. A copy of the signal is directly sent back at the analog output. The phase difference measurement takes place in the first FPGA.

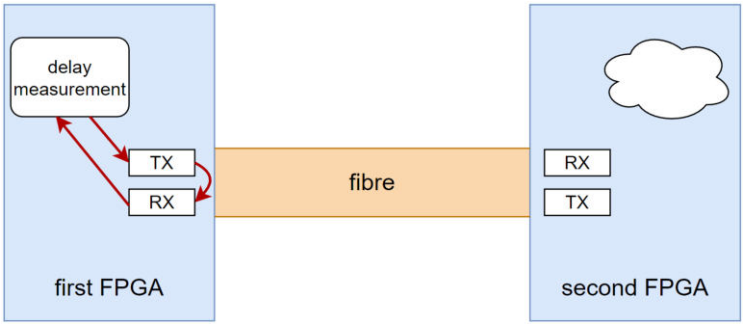

Figure 3.6: Local loopback: the signal from the first FPGA reaches the transmitter of the SerDes. A copy of the signal is directly sent back within the first FPGA. The phase difference is measured within the FPGA.

3.3 Measuring Method

The measurement of the total timing delay is split into two delays: the coarse time Δt_c and fine time Δt_f. The sum of these two delays is the total delay Δt_{total}:

$$\Delta t_{total} = \Delta t_c + \Delta t_f \tag{3.1}$$

3.3.1 Coarse Time

The method of the coarse time measurement is illustrated in the time response diagram 3.7. The rising edge of the central clock from the FPGA samples the transmitted pulse. With the next rising edge of the clock, a counter is activated. The counter increments by one for each clock cycle, starting from zero. When the pulse returns, the current count value c is saved. The coarse time can then be estimated using the following equation:

$$\Delta t_c = 8\,\text{ns} \cdot c \tag{3.2}$$

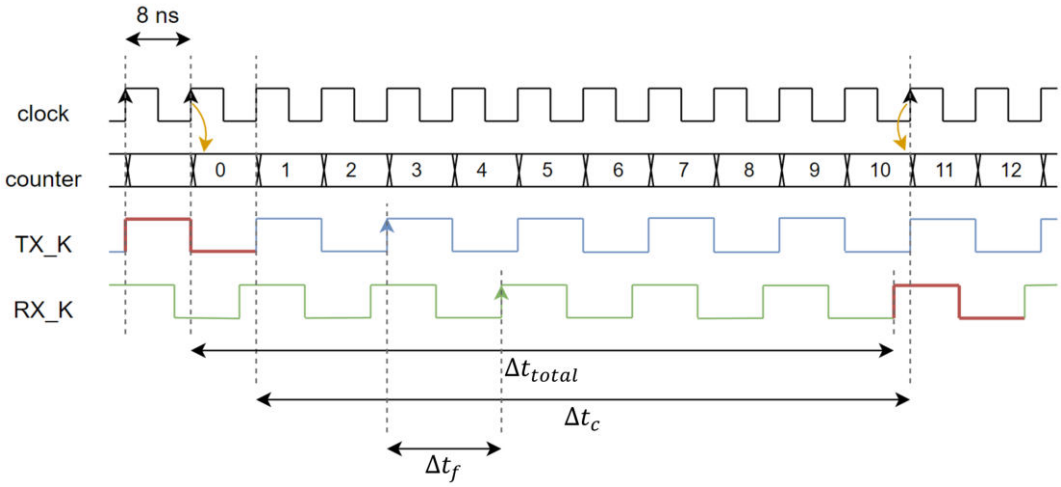

Figure 3.7: Scheme illustrating the delay measurement. The pulse is depicted in red and embedded into the transmitting K-character TX_K, it comes back with the data stream in the receiver (RX_K). For the coarse time Δt_c, the outgoing signal gets sampled with the central clock. A counter starts counting with the rising edge of the next clock cycle. The count is saved when the signal comes back, providing the coarse delay time. The fine time Δt_f is estimated between two subsequent rising edges of TX_K and RX_K.

3.3.2 Fine Time

The outgoing and incoming signals are embedded into the K-Characters TX_K and RX_K of the data stream, making the fine time measurement independent of the actual pulse. The fine time is determined as the difference between a rising edge of the TX_K channel and the subsequent rising edge of the RX_K channel, as depicted in figures 3.7 to 3.9. This is possible because they both have the same frequency: $\nu_K = 62.5\,\text{MHz}$ ($T_K = 16\,\text{ns}$), ensuring a constant phase difference between them, which allows measurement at any time (see figure 3.8).

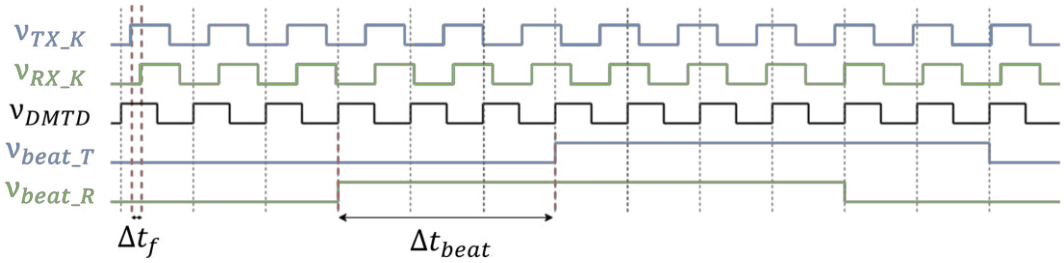

Figure 3.8: Time response diagram of the 'Digital Dual Mixer Time Difference'-method, illustrating the stretching of K-Character signals using coupled D-FFs. In blue the transmitted signal ν_{TX_K} is transformed into ν_{beat_T} by one D-FF, stretching the signal. Similarly, in green the received signal ν_{RX_K} undergoes the same process, resulting in a phase difference Δt_{beat} between the two K-Characters which can be translated back to Δt_f.

To measure this phase difference, we utilize a method called 'Digital Dual Mixer Time Difference' (D-DMTD) which is illustrated in figure 3.8 [22]. With D-DMTD it is possible to measure a greater resolution than the 8 ns coming from the central clock. The two K-Character signals with the frequencies ν_{RX_K} and ν_{TX_K} pass through coupled D-FF and are sampled by a clock with a slightly lower frequency ν_{ddmtd}, calculated using the following equation:

$$\nu_{ddmtd} = \frac{N}{N+1} \cdot \nu_K \text{ [22].} \tag{3.3}$$

After passing the D-FF, the initial frequencies get stretched out in time and receive new frequencies ν_{beat_T} and ν_{beat_R} (figure 3.8). Half a period of the new frequency ν_{beat} equates to N-times the clock frequency ν_{ddmtd}. In our case, N is set to 624, resulting in $\nu_{ddmtd} = 62.4\,\text{MHz}$. This choice provides a fine resolution for the smallest possible time step $\Delta t = 25.6\,\text{ps}$, which is given by:

$$\Delta t = \frac{1}{N \cdot \nu_K} \text{ [22].} \tag{3.4}$$

With the stretched signal, the beat measurement is performed between the rising edge of the stretched TX_K signal and the subsequent rising edge of the stretched RX_K signal. This yields Δt_{beat} which can be used to calculate the actual fine time Δt_f with the following equation:

$$\Delta t_f = \Delta t_{beat} \cdot \left[1 - \frac{N}{N+1}\right] \text{ [22].} \tag{3.5}$$

This beat measurement differs from the approach for assessing the phase difference between the stretched-out signals in the reference paper. In the reference paper, the phase difference is estimated using an exclusive OR (XOR; table 3.1) operation between the two rising edges of the signal [22]. In contrast, our measurement exclusively performs a beat measurement between the rising edge of the incoming (TX_K) signal and the rising edge of the outgoing (RX_K) signal. This beat measurement enables identifying the order of the edges of the stretched-out signals and provides values between 0 ns and 16 ns instead of values up to only half the K-Character frequency. Figures A.7 to A.16 in the appendix show the evolution of the phase difference between the two outstretched signals.
Both output signals, ν_{beat_T} and ν_{beat_R}, may contain an unpredictable number of glitches caused by environmental noise or jitter. These glitches can hinder the detection of the true rising edge. Therefore, a deglitching algorithm removes them. However, this process may shift the edges slightly from their 'real' positions, introducing measurement inaccuracies[22]. To mitigate this issue, multiple measurements are conducted (in total 2^{18}), resulting in a histogram of fine times resembling a Gaussian distribution. By calculating the average value, a more accurate estimation of the fine time is obtained.
Initially, we encountered inconsistencies between the total delay measured with the oscilloscope and the measurement within the FPGA. The following section discusses these discrepancies and presents solutions to address the challenges.

3.3.3 Challenges

The deviation between the two measured delays in the oscilloscope and FPGA showed a certain regularity: the difference was consistently a multiple of eight (see figure A.17). Based on this information, we identified two problems, which are discussed in the subsequent paragraphs: one will be referred to as 'Fine Time Range Adjustments' and the other as 'Wrong Coarse Time'. Additionally, we encountered three other discrepancies, which will be explained and discussed in the following paragraphs.
By addressing these challenges and finding suitable solutions, we aim to improve the accuracy and reliability of our timing measurements for P-ONE.

Fine Time Range Adjustments The fine time measurement produces values between 0 ns and 16 ns. This range is a natural consequence of measuring the phase difference between the transmitted and received K-Characters, which operates with half the clock frequency (62.5 MHz). As a result, their periodic time is 16 ns. However, this implies that sometimes the measured value exceeds 8 ns, which is the resolution of the coarse time measurement. Consequentially, the fine time occasionally adds 8 ns excessively to the total delay. Figure 3.9 illustrates this scenario. As a solution, the fine time needs to be adjusted by subtracting 8 ns whenever it exceeds that value.

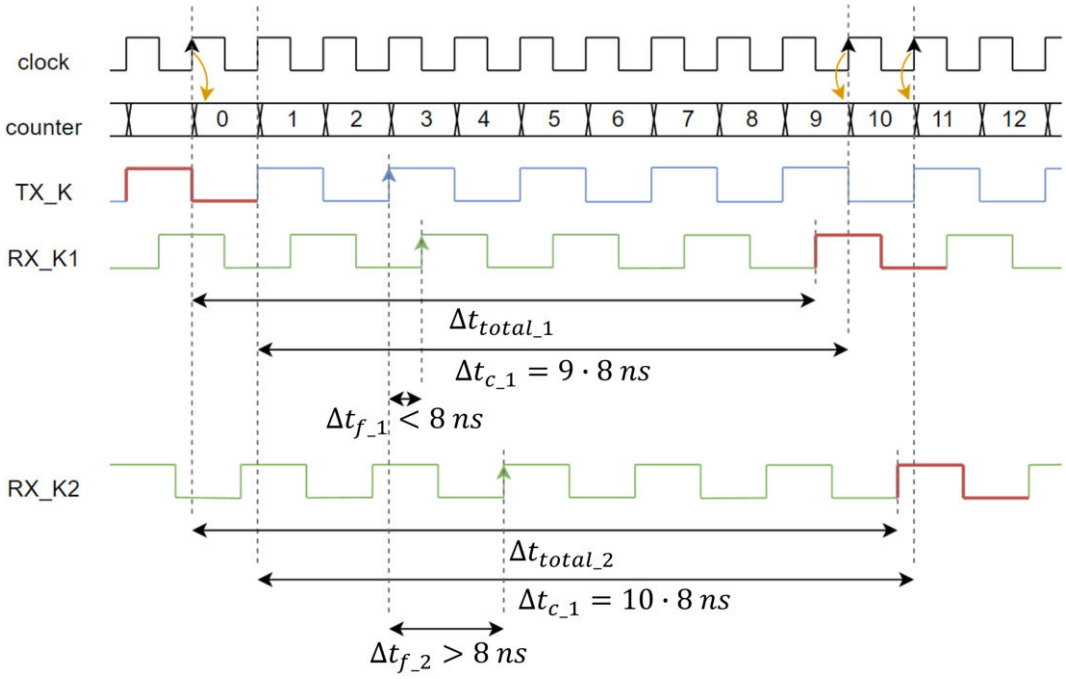

Figure 3.9: Conceptual representation of the fine time range-issue: the outgoing signal (red) is embedded into the blue TX_K-Character. The first yellow arrow indicates the count-start and the two arrows on the right illustrate the saving of the clock counter once the signal returns (green). In the first case (RX_K1), the fine time does not exceed 8 ns, providing an accurate total time when adding to the coarse time. In the second case (RX_K2), the phase shift between the outgoing and incoming signal exceeds 8 ns causing an increased counter for the coarse time as well, resulting in an overestimated total time.

Wrong Coarse Time Occasionally, the coarse time is found to have a 8 ns offset (figure 3.10). This deviation arises from the location of the coarse time measurement

within the fabric of the FPGA. The logic implementing the measurement is not ideally positioned, resulting in a longer signal path and a delay of one clock cycle. This delay adds 8 ns to the coarse time value. Once identified, the coarse time needs to be adjusted. This discrepancy can be avoided by setting constraints for the location of the coarse time measurement while programming the FPGA.

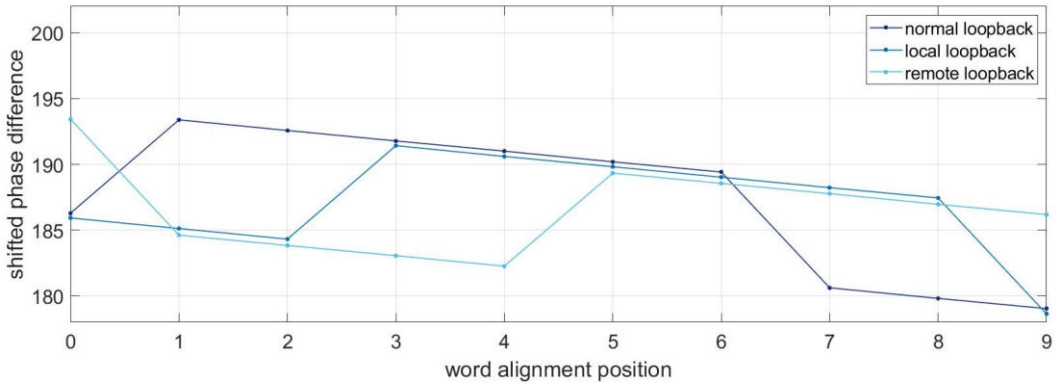

Figure 3.10: Phase difference of the 150 m fiber length for various word alignment positions, with the delay adjusted to enhance the visibility of the dependency. The 8 ns discrepancy from the fine time measurement was adjusted. Still, each of the three measurements exhibits a notch in its graph, highlighting the 8 ns discrepancy in the coarse time measurement.

Inaccurate Fine Time near the Extremes Furthermore, we found that when the fine time measurement approached 0 ns or 16 ns, irregular distributions occurred, as shown in figure 3.11. In the fine time measurement process, the signals are deglitched, which can lead to jumps in the measured values between slightly above 0 ns and slightly below 16 ns. Averaging such results no longer provides a precise phase difference. To address this issue, we shift the measurement to a more stable word alignment position. If the measurement is shifted to other word alignment positions, the phase measurement would require adaptation by $n_{\mathrm{WAP}} \cdot 800\,\mathrm{ps}$.

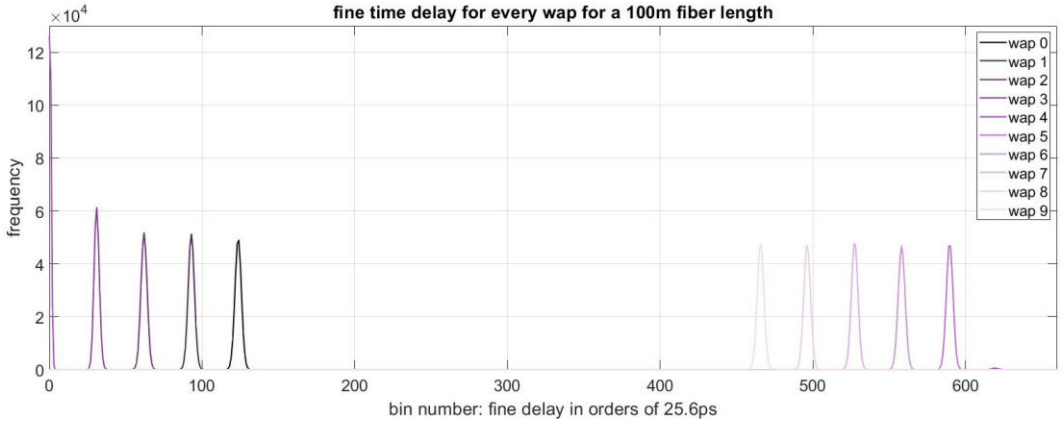

Figure 3.11: Histogram of the fine time measurement for the 100 m fiber length depicting every word alignment position (wap). The peak for wap 4 is significantly higher and not Gaussian-shaped. Additionally, a very small peak on the right side of the figure indicates that the deglitching caused jumps in the phase difference, making the estimation of a precise difference via averaging no longer possible.

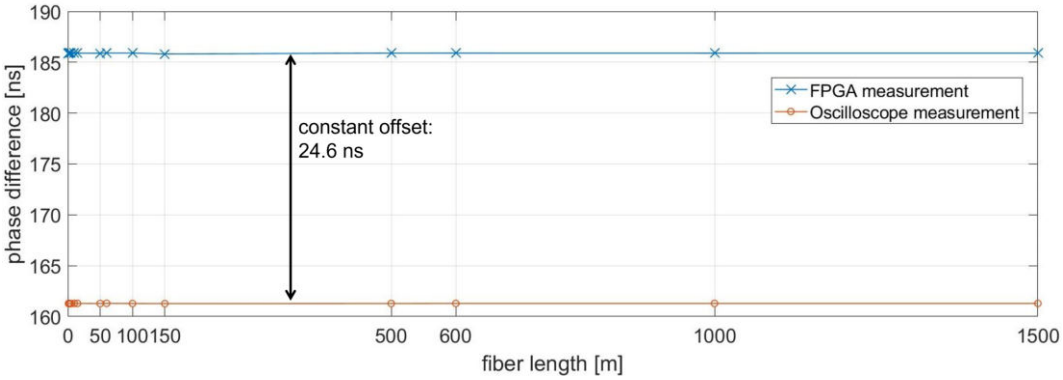

Figure 3.12: Local loopback delay measurement for different fiber lengths. As the local loopback delay remains the same for each fiber the general offset of 24.6 ns between the FPGA and Oscilloscope measurement is visible.

General Offset Comparing the resulting delays for different fiber lengths obtained from the oscilloscope measurements and the internal FPGA measurement, we observe a constant offset of 24.6 ns. Several factors could contribute to this offset, including differences in the lengths of the cables connecting the oscilloscope to the setup or routing within the TRB3sc board and the FPGA. However, the influence of the cable length difference is expected to be minimal. In contrast, the routing within the

board and FPGA likely contribute significantly to this offset. As depicted in figure 3.12 and 3.16, the offset remains constant within the range of measurement errors. Considering that this measurement solely yields relative time values, the presence of an offset does not cause significant concern, as it results in a shifted delay rather than incorrect delays.

Unidentified Offset for Different WAPs Figure 3.13 illustrates that the local loopback measurement deviates for word alignment positions greater than two, the normal loopback deviates from word alignment position one and the remote loopback exhibits a deviation from word alignment position five even after the fine and coarse time were adapted. This offset is approximately 150 ps for every measurement. It is still under investigation and requires further analysis to determine its cause.

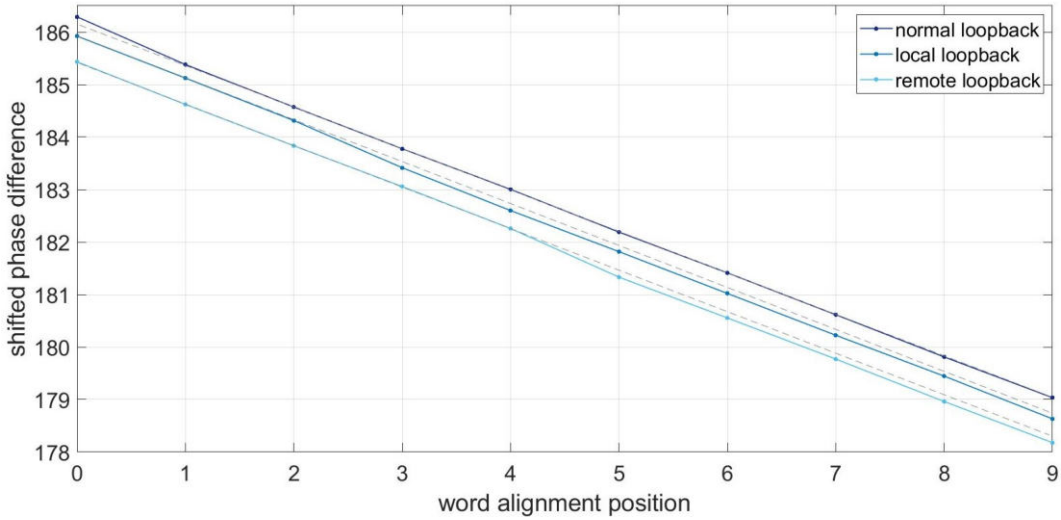

Figure 3.13: Phase difference of the 150 m fiber length for the different word alignment positions. The delay is adapted to make the dependency visible. Even after adapting the 8 ns to the fine and coarse time, a small offset in all three graphs is visible. This depicts an offset of 150 ps which has not yet been determined.

3.4 Results

This chapter presents the results of delay measurements for different fiber lengths, ranging from 1 m to 1500 m, comparing the measurements of the oscilloscope with the measurement within the FPGA, as explained in the previous section. Additionally, the reliability of the FPGA measurement will be discussed.

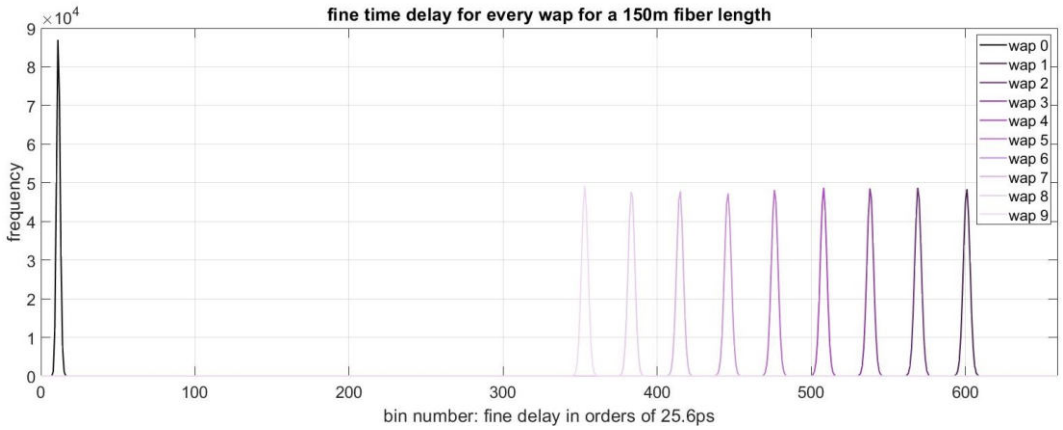

Figure 3.14: Histogram of the fine time measurement for the 150 m fiber length depicting every word alignment position (wap). The peak for wap 0 is significantly higher than every other peak, indicating that the fine time for wap 0 may not be accurate. Thus a wap-shift for the measurement is necessary.

For each delay the coarse time and fine time value were adjusted if the aforementioned challenges were encountered. In all measurements, except for the 150 m fiber, the word alignment position was set to 0. For the 150 m fiber a word alignment position of 3 was chosen, because the peak for word alignment position 0 shows an irregularity (figure 3.14). Thus, the 150 m delay was adjusted by adding three times 800 ps to ensure comparability with the other measurements.

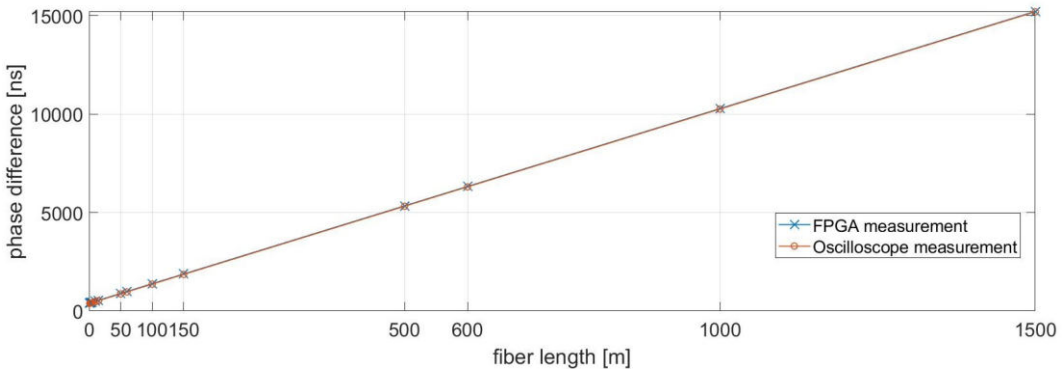

Figure 3.15: Results for the normal loopback delay for different fiber lengths. Both, the FPGA and oscilloscope measurements grow linearly with increasing fiber length. The offset between the two measurements is not visible due to the dimension of the delays for long fibers.

Figure 3.15 depicts the phase differences obtained from the FPGA and oscilloscope measurements for the different fiber lengths. As expected, the phase difference increases with the length of the fiber while the offset remains constant at 24.6 ns. The offset is not visible in figure 3.15, because it is small compared to the measured delays. Thus figure 3.16 and 3.17 further illustrate this offset. Within the errors (uncertainties are discussed in section A.3) the deviation of the FPGA and oscilloscope measurement remains constant for all fiber lengths. Also, the proportion of the two measurements shows the constant offset. The proportion of the remote loopback and normal loopback increases because the offset remains constant but the delays increase. The proportion of the local loopback remains constant because, for each fiber length, the local loopback delay should be the same as well as the offset, providing the depicted graph.

The presented plots and results confirm the reliability of the FPGA measurement method. The FPGA measurements show consistency with the oscilloscope reference, with only a constant offset differentiating the two. Therefore, these findings indicate the high dependability and effectiveness of the FPGA-based measurement approach.

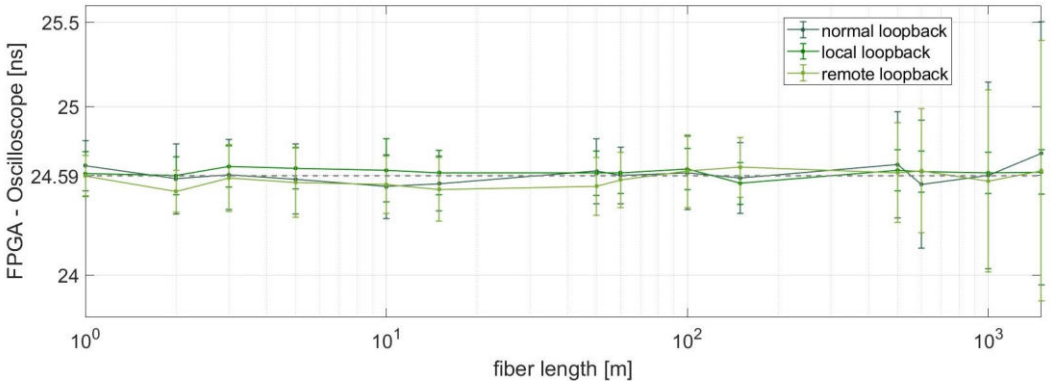

Figure 3.16: The difference between the FPGA and oscilloscope measurement for each of the three measurements. Within the errors of the measurement, this graph shows the constant offset between the FPGA and oscilloscope measurement of 24.6 ns.

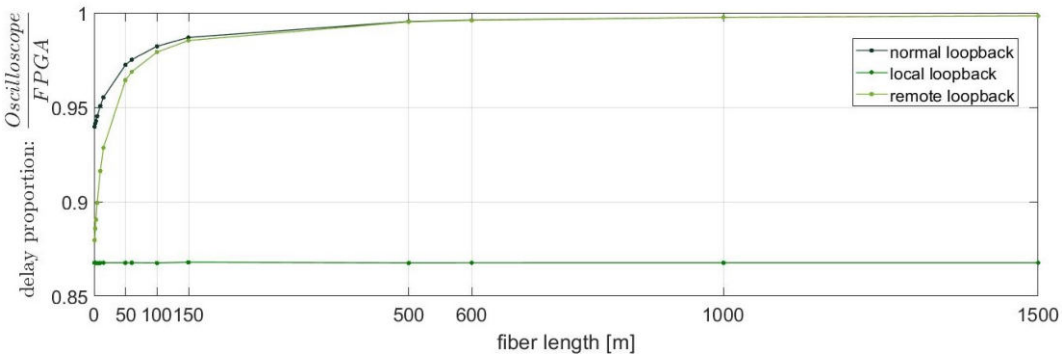

Figure 3.17: These three graphs depict the proportion of the oscilloscope and FPGA measurement. While the proportion is constant for the local loopback delays since they are approximately the same for each fiber, the normal and remote loopback proportions increase with greater lengths because the offset is constant and the delays increase with the fiber length.

Chapter 4

Conclusion and Outlook

4.1 Development of a Production Process for the Optical Module

A suitable integration method for the mass production of optical modules that meets the optical requirements has been identified by iteratively coupling PMTs to a prototype hemisphere with gel pads. The use of a mold integrating the PMT directly in the gel pad production process has made the coupling to the PMT faster and more feasible. The integration of this PMT-gel pad structure works best by using a syringe for pouring the gel onto the glass. Wacker Elastosil RT 601 is more effective for removing PMTs compared to the tackier main gel pad component Wacker Silgel 612. With 7 g interface gel, the current design of gel pads couples fully to the glass of the hemisphere, leaving a small brim of gel on the sides. Ongoing investigations are focused on assessing the photon acceptance of the optical module with the overflow brim.
Moving forward, several key steps need to be taken in the development of the optical module and integration process. The alignment of the hemisphere needs further development, as it is crucial to ensure an even flow of gel for an evenly distributed gel brim. Further investigation is needed to understand and address the presence of tree-like structures and strange gel borders, evaluating their potential negative impact on the optical properties and photon acceptance of the module, and exploring ways to mitigate these effects. Testing the optical module with working PMTs is essential to gather data on angular acceptance. Additionally, shake tests should be conducted to assess the resilience of the optical modules to vibrations encountered during transportation and deployment. Once the gel pad design and integration method are reviewed, the production of optical modules for P-ONE-1 can commerce. It is crucial to develop efficient mass production procedures, optimizing production speed while ensuring product quality and consistency in the performance of each module. The first step towards developing a production process for optical modules was creating a suitable, dust-free environment by constructing a clean room.

4.2 Understanding the Operation of the Timing System in the Ocean

To conclude the second topic of this bachelor thesis, different optical fiber lengths were used for delay measurements within an FPGA. The results were compared to oscilloscope measurements to analyze the reliability of the FPGA-based measurement. We identified a consistent difference between the two measurements with a multiple of 8 ns and addressed the challenges that go along with it. The results demonstrate that the FPGA measurements closely align with the oscilloscope reference, apart from a constant offset. Therefore, the FPGA measurements proved to provide accurate timing information for the P-ONE system. This enables synchronization of the collected data from each optical module of P-ONE.
Once the P-ONE-1 and its timing system operate in the Pacific Ocean, several challenges may occur and require examination beforehand. The effects of temperature on the FPGA measurement need to be investigated in order to understand their impact on time synchronization. The optical modules will likely reach thermal equilibrium after deployment in the ocean, where the heat produced inside the optical modules is balanced by the surrounding water. Since FPGAs are sensitive to temperature changes, this will possibly implicate slightly different timing delays and create another offset source. Remeasuring the timing delays once deployed in the ocean is necessary either way, as the then straightened cables in P-ONE induce changes in the timing delay compared to the previously bent fibers. Furthermore, the impact of pressure on the optical fibers in the deep ocean needs to be examined to gain an understanding of the system's performance and reliability. Lastly, the unresolved shift of 150 ps for different word alignment positions requires further investigation. It could prove advantageous to determine its origin and asses its impact on the delay measurement accuracy.

Appendix A

Appendix

A.1 Pictures of P-ONE, the Optical Module and Integration Process

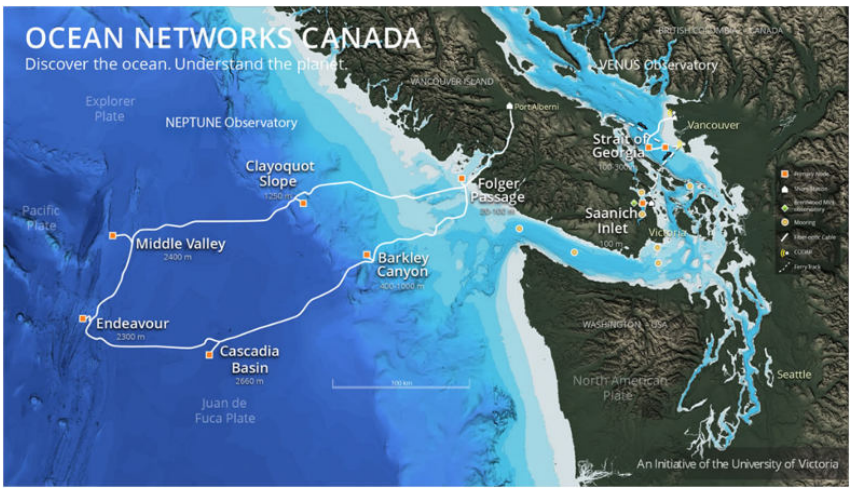

Figure A.1: The NEPTUNE observatory from Ocean Networks Canada offshore Vancouver Island. The P-ONE will be located at the node at Cascadia Basin [9].

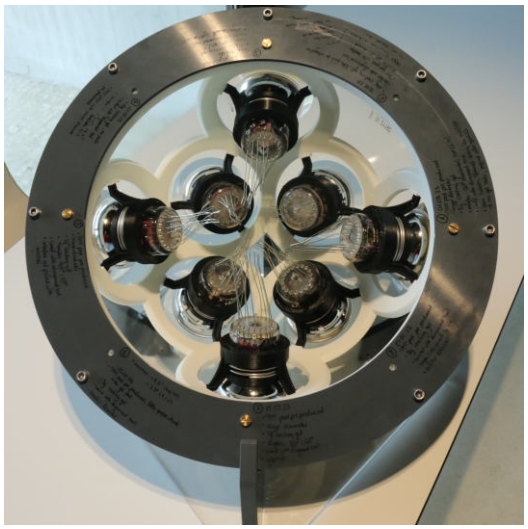

Figure A.2: Internal view of a fully integrated prototype optical module hemisphere.

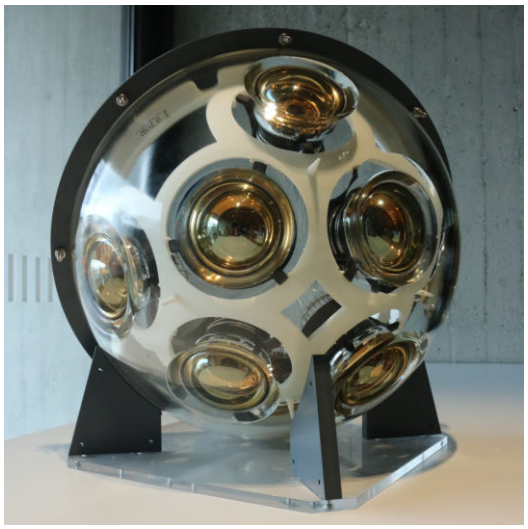

Figure A.3: External view of the fully integrated prototype optical module hemisphere.

Figure A.4: View from the outside of the vacuum chamber. The automatic stirring device mixes the gel gel while degassing.

Figure A.5: The syringe is drawn up to more than 7 g. With a small amount of gel this must be done carefully to not produce bubbles in the process.

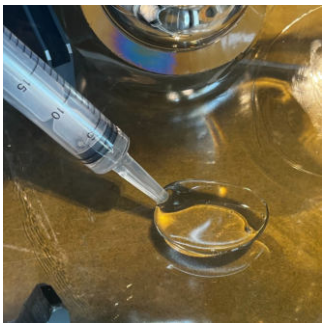

Figure A.6: With the syringe the right amount of gel can be poured onto the glass surface more easily. For test purposes the frame is not applied on this hemisphere.

A.2 Delay Measurement Results and Plots

A.2.1 Phase Shift for Different Word Alignment Positions in the Outstretched Signal for 15 m fiber

The following screenshots showcase the outstretched signals for the 15 m fiber on the oscilloscope, illustrating the variation of the phase difference in the fine time measurement for different word alignment positions (WAPs). In each measurement, the outgoing signal (represented in orange) remains constant, and the incoming signal (depicted in blue) shifts more to the left for each word alignment position. The suspected issue of exceeding the outgoing signal, causing an inaccurate measurement does not occur (see section 3.3).

Figure A.7: WAP 0

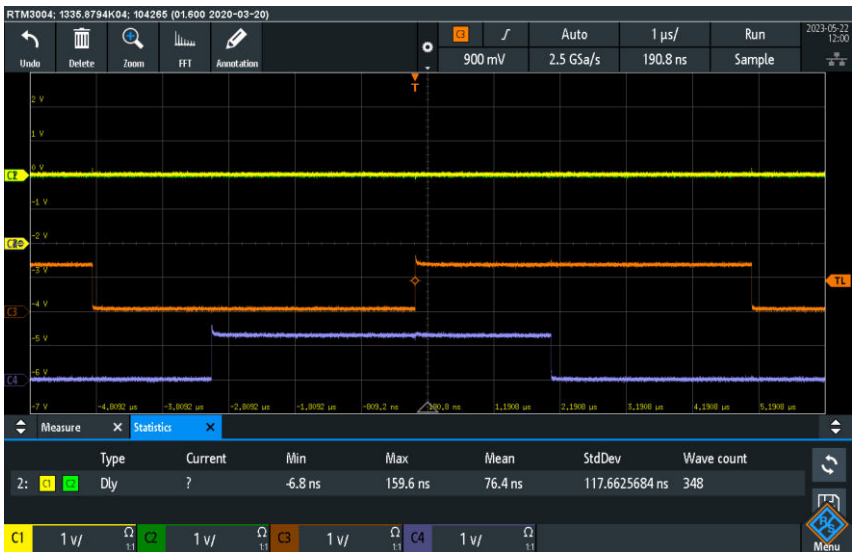

Figure A.8: WAP 1

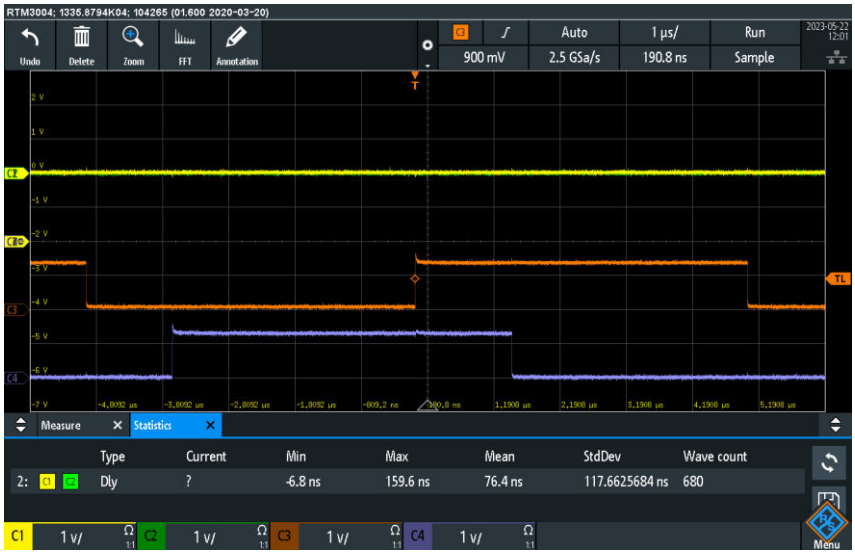

Figure A.9: WAP 2

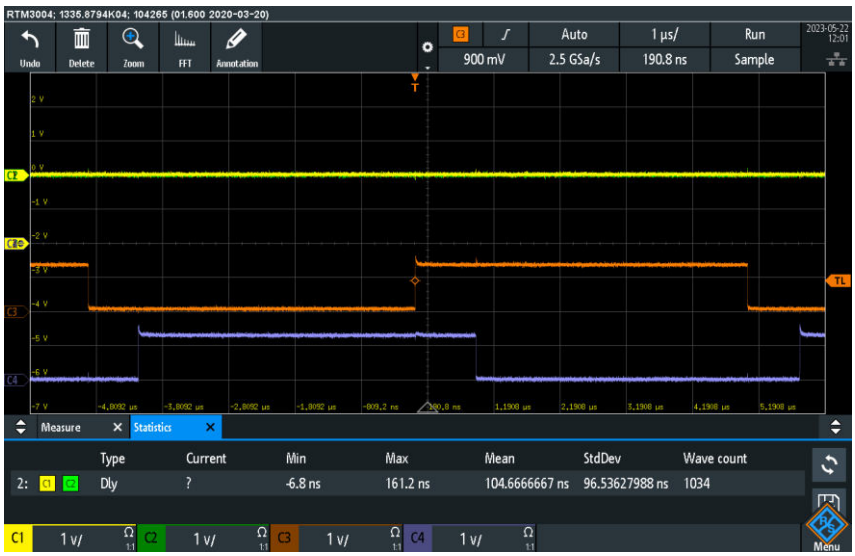

Figure A.10: WAP 3

Figure A.11: WAP 4

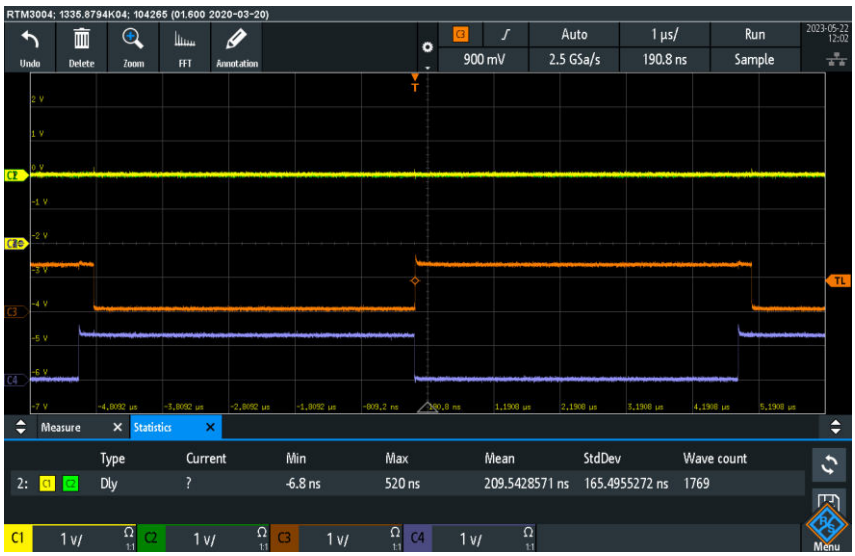

Figure A.12: WAP 5

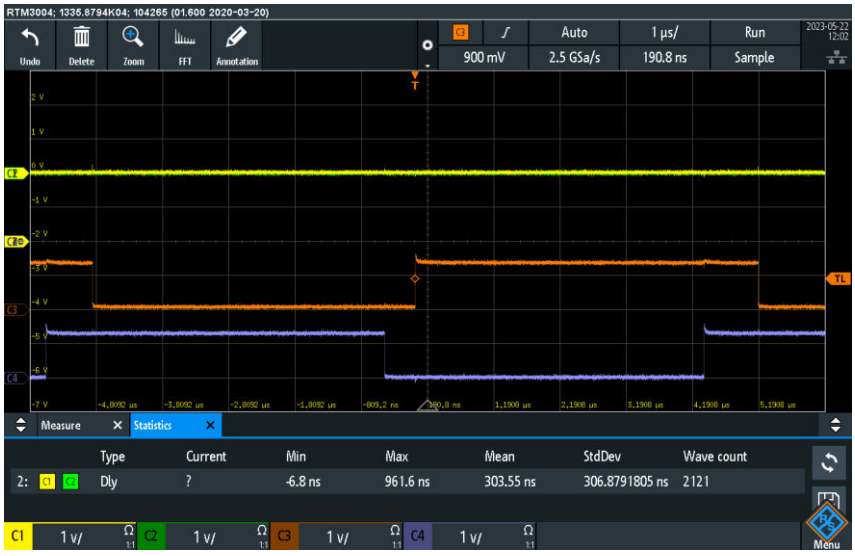

Figure A.13: WAP 6

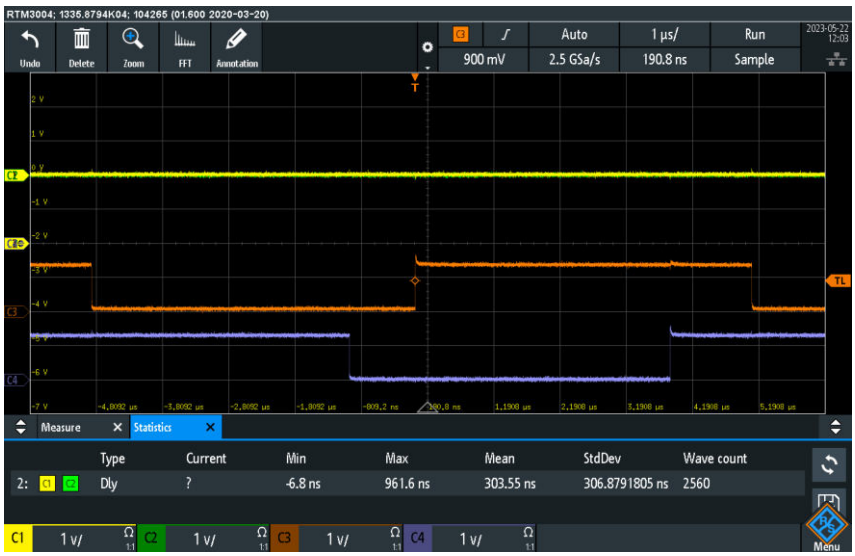

Figure A.14: WAP 7

Figure A.15: WAP 8

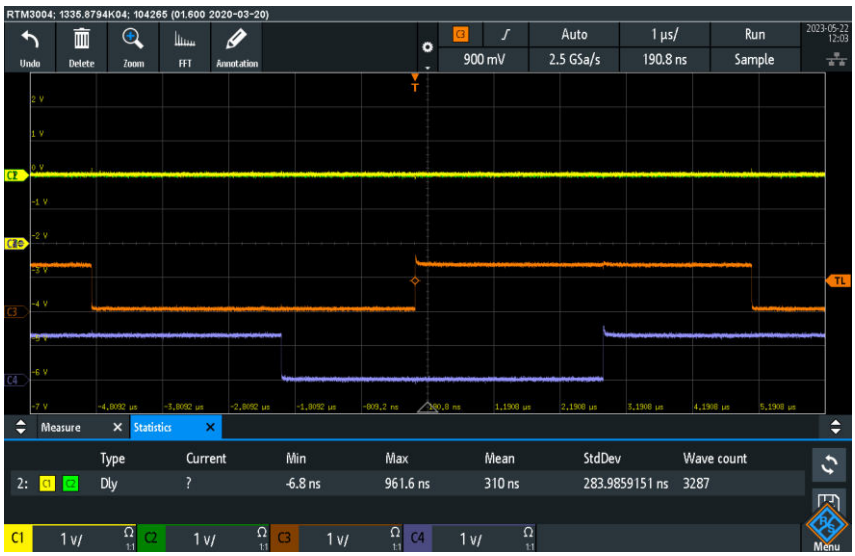

Figure A.16: WAP 9

A.2.2 Example for the 8 ns shifts from the coarse time and fine time for the 150 m fiber

The following three graphs exemplify the adjustments for the fine time and coarse time which were described in section 3.3.3. The delays are shifted for visual reasons and are plotted against the word alignment positions. After adjusting the fine time, a 8 ns offset is still visible in figure A.18. After correcting this shift coming from the coarse time, the still unidentified 150 ps shift is visible.

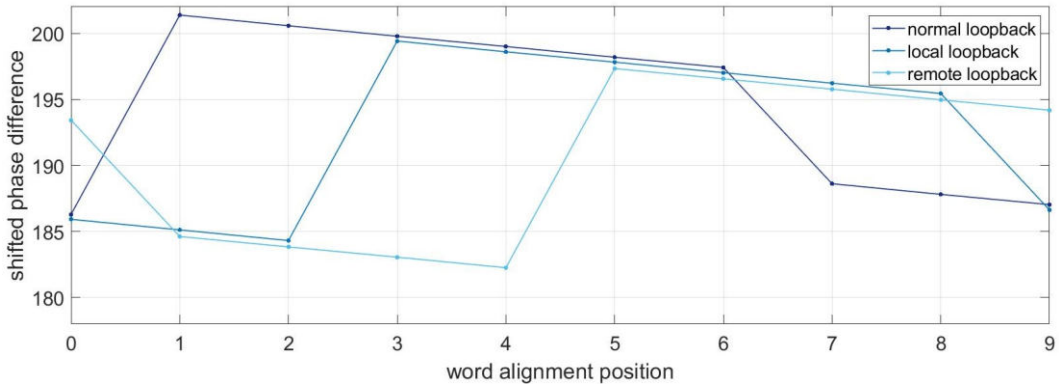

Figure A.17: No delays adjusted.

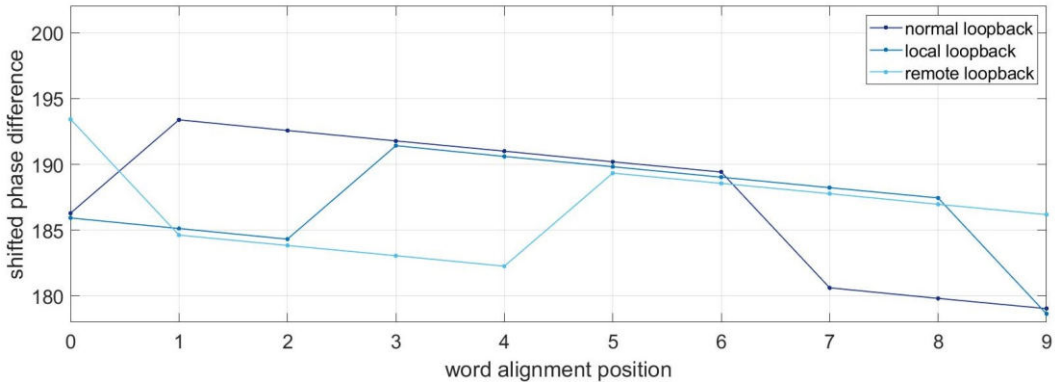

Figure A.18: Fine time adjusted to be between 0 ns and 8 ns.

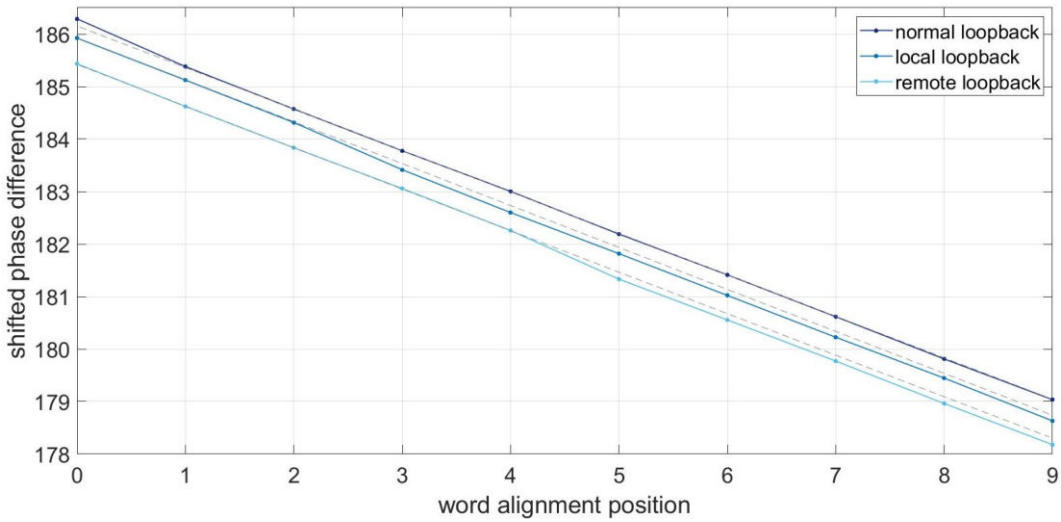

Figure A.19: Fine time and coarse time adjusted. 150 ps offset still visible.

A.2.3 Histogram plots for every fiber length and all word alignment positions

The following plots depict histogram curves for the different fiber lengths. Each peak resembles the frequency of hits for a certain phase difference. The peaks from darker to lighter purple depict the different word alignment positions from 0 to 9. The histograms exhibit a consistent pattern with no noticeable irregularities at word alignment position 0, except for the 150 m fiber length. In this case, the histogram reveals a higher peak at word alignment position 0 compared to the other positions,

generating an inaccuracy with the mean value of the measurement. To address this issue, we shifted this measurement to the more stable word alignment position 3.

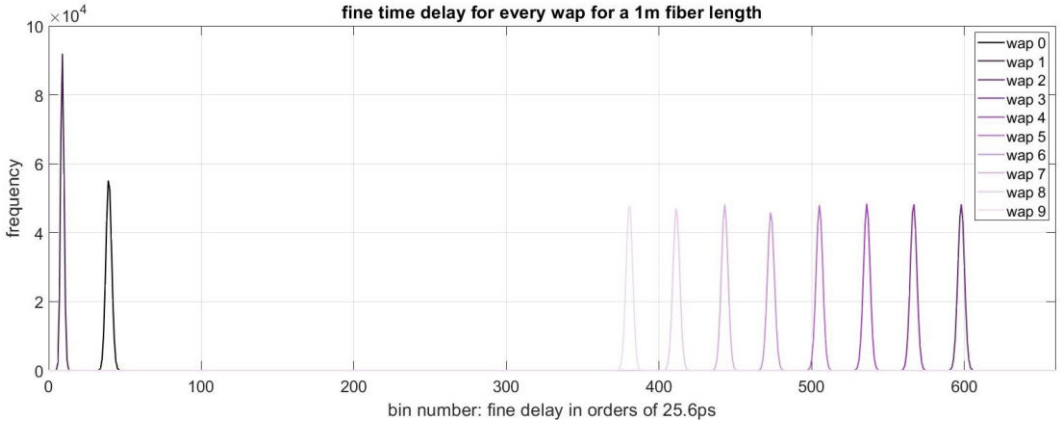

Figure A.20: 1 m fiber

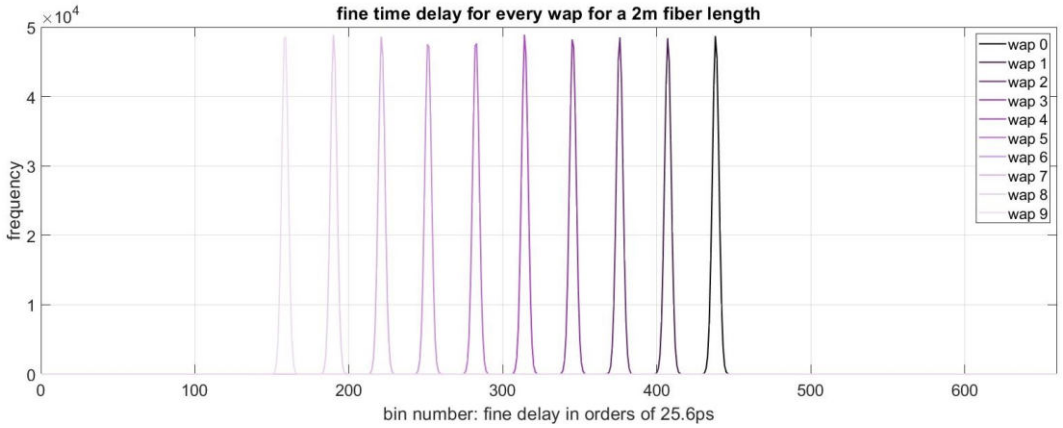

Figure A.21: 2 m fiber

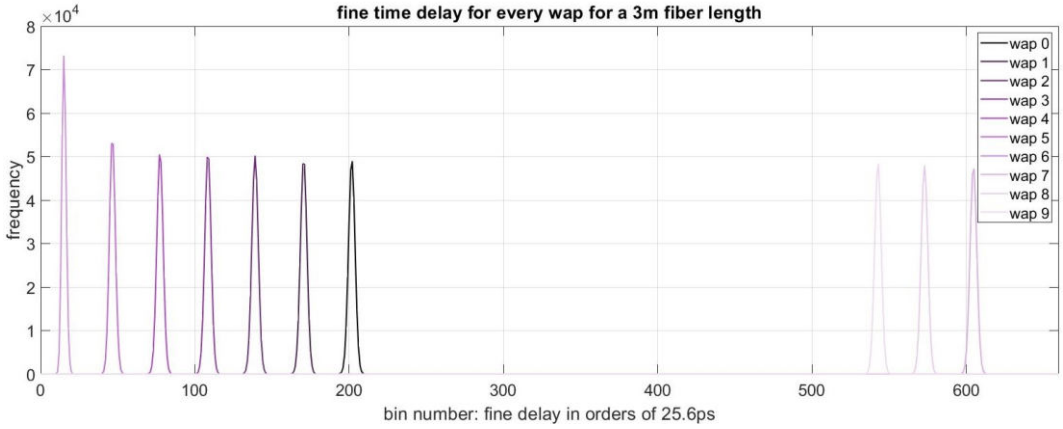

Figure A.22: 3 m fiber

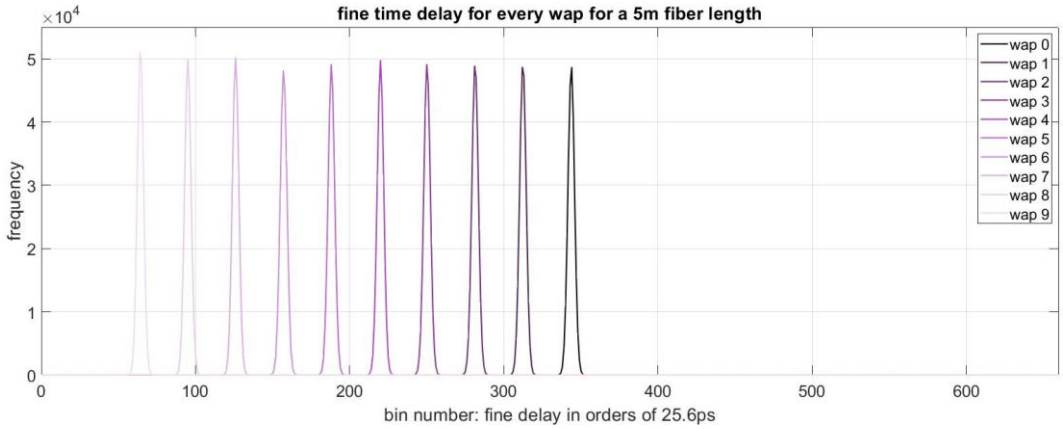

Figure A.23: 5 m fiber

Figure A.24: 10 m fiber

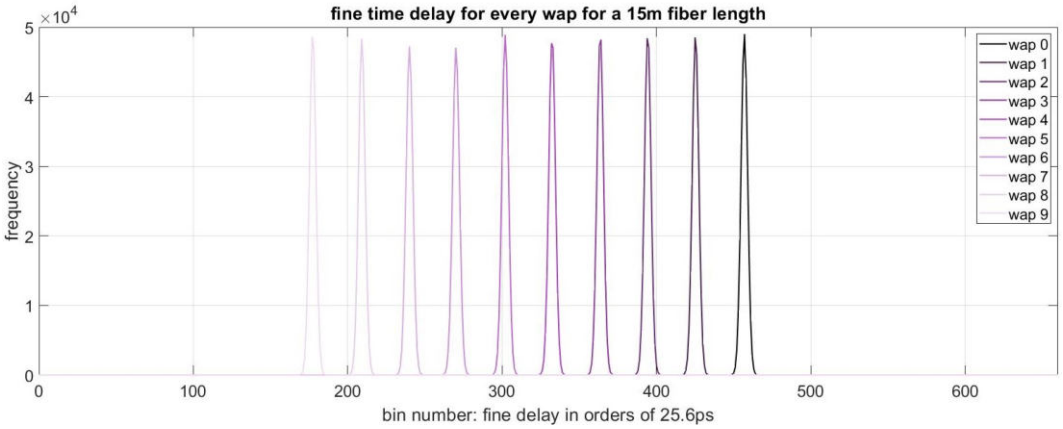

Figure A.25: 15 m fiber

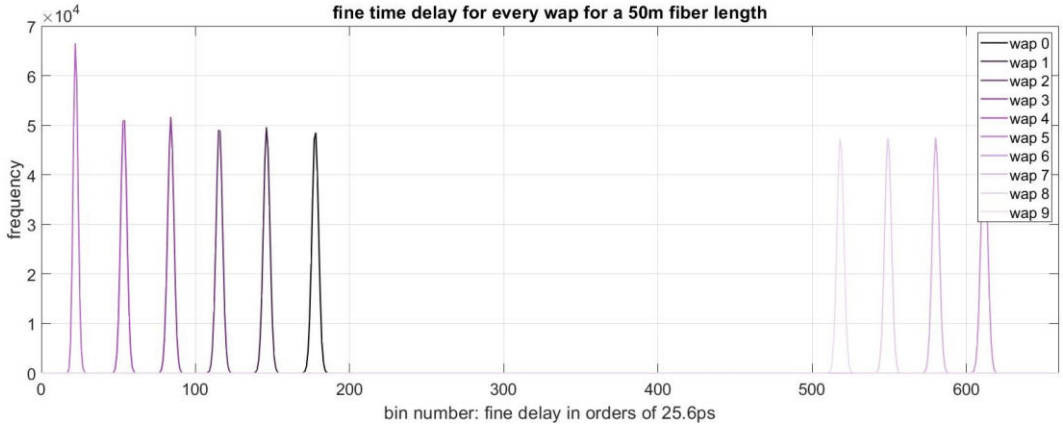

Figure A.26: 50 m fiber

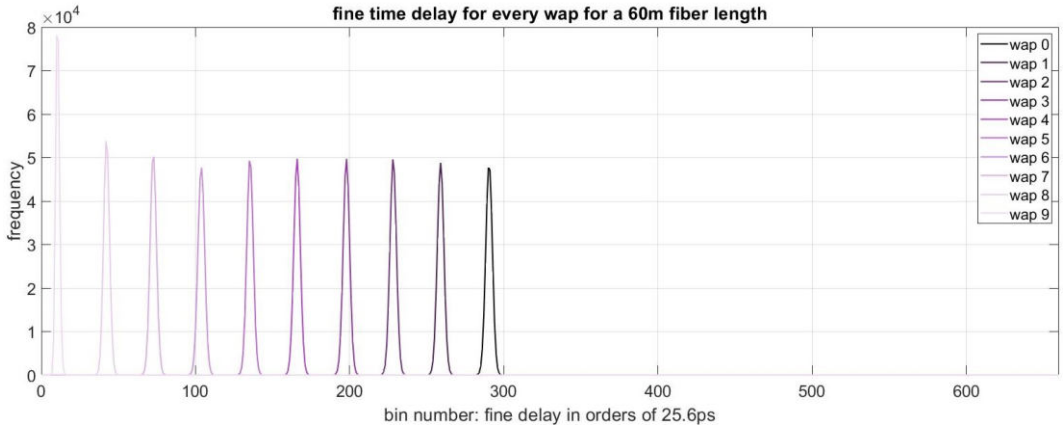

Figure A.27: 60 m fiber

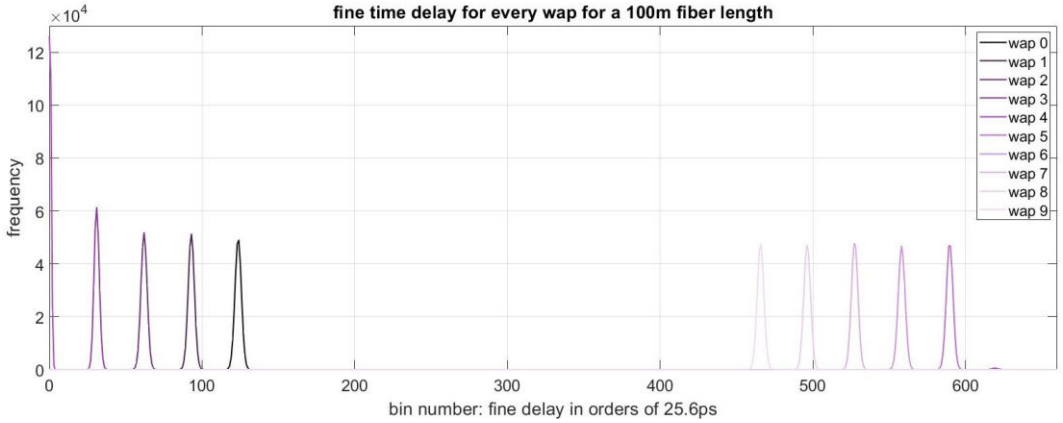

Figure A.28: 100 m fiber

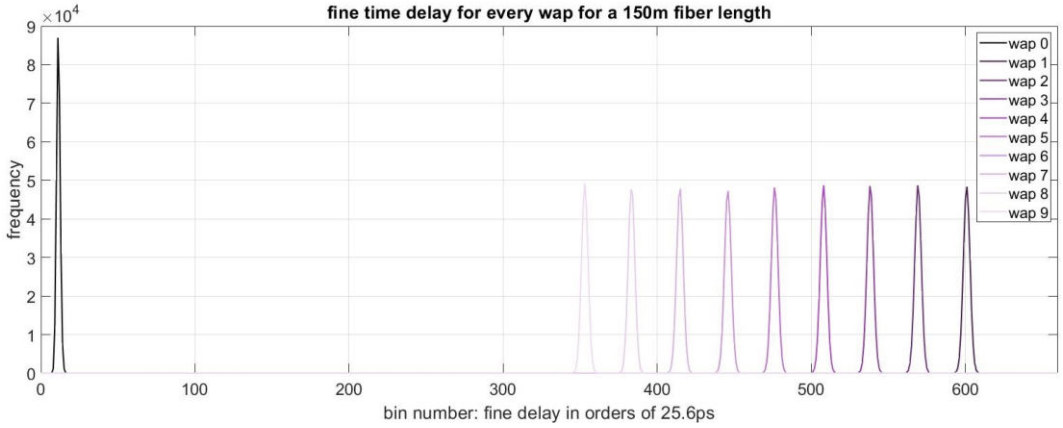

Figure A.29: 150 m fiber

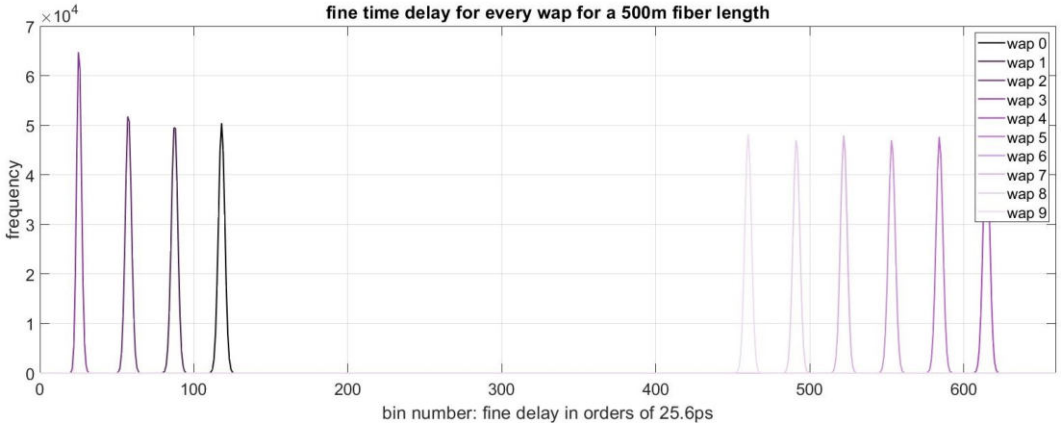

Figure A.30: 500 m fiber

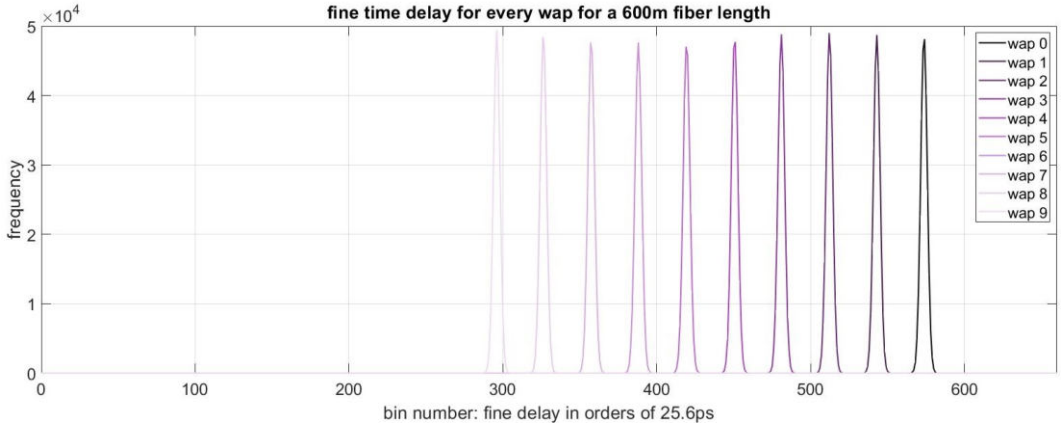

Figure A.31: 600 m fiber

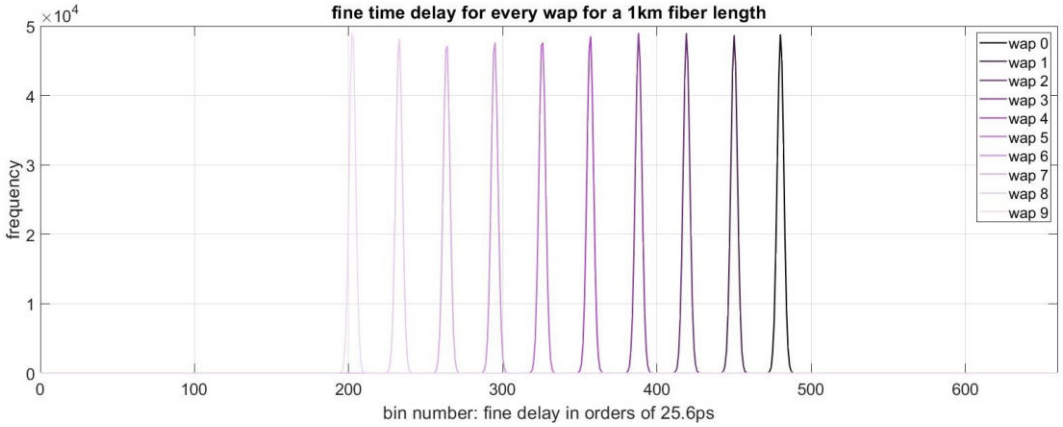

Figure A.32: 1000 m fiber

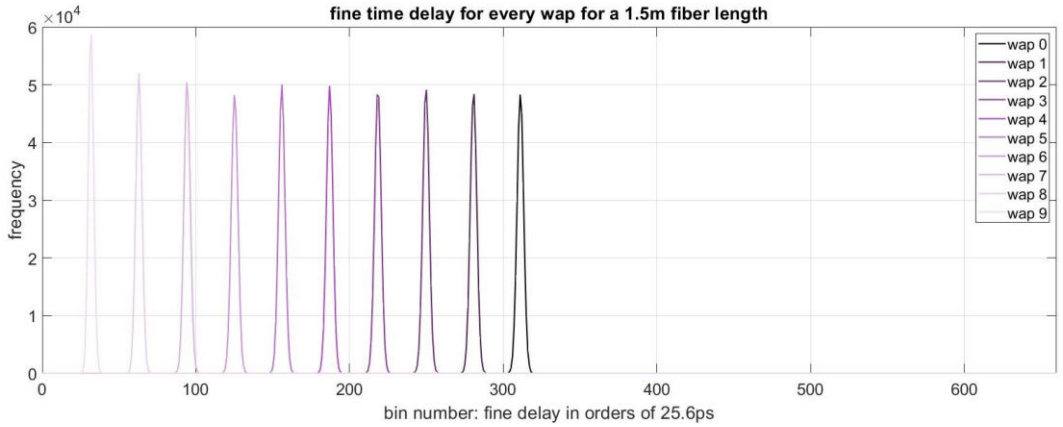

Figure A.33: 1500 m fiber

A.2.4 Delays for every fiber length

Table A.1 presents the delay values obtained for each fiber length from the measurement described in section 3.4. The values were adjusted using the methodology outlined in section 3.3 which provides table A.2. If not indicated otherwise, the unit used for these two tables is ns. The abbreviations nlb, llb, and rlb stand for 'normal loopback', 'local loopback', and 'remote loopback', O and F depict the oscilloscope or FPGA measurement.
Using the adapted values from table A.2 three plots can be generated: the normal loopback, remote loopback, and the local loopback delay. Each plot depicts the oscilloscope and FPGA measurement.

l [m]	O_nlb	F_nlb	O_llb	F_llb	O_rlb	F_rlb
1	384.39	409.0390	161.28	185.8810	179.58	212.1683
2	394.65	427.2203	161.30	185.8899	189.86	230.3570
3	404.56	437.1562	161.27	185.9142	199.73	232.3047
5	424.23	456.7991	161.28	185.9139	219.40	259.9504
10	473.31	505.8344	161.29	185.9108	268.44	308.9770
15	523.14	563.6827	161.29	185.8973	318.32	358.8289
50	867.92	900.5364	161.28	185.8855	663.16	695.6878
60	966.82	999.4111	161.30	185.9070	762.00	794.5652
100	1362.58	1387.1865	161.28	185.9089	1157.74	1190.3563
150	1853.22	1893.7951	158.87	199.4140	1648.42	1673.0599
500	5314.41	5339.0649	161.28	185.9018	5109.60	5142.2079
600	6302.16	6342.6993	161.29	185.9044	6097.36	6121.9796
1000	10251.72	10292.3106	161.29	185.8974	10046.90	10087.4583
1500	15191.26	15223.9824	161.29	149.9014	14986.50	15019.1192

Table A.1: Initial values for the delay measurement in [ns] if not indicated otherwise.

l [m]	O_nlb	F_nlb	O_llb	F_llb	O_rlb	F_rlb
1	384.39	409.0390	161.28	185.8810	179.58	204.1683
2	394.65	419.2203	161.30	185.8899	189.86	214.3570
3	404.56	429.1562	161.27	185.9142	199.73	224.3047
5	424.23	448.7991	161.28	185.9139	219.40	243.9504
10	473.31	497.8344	161.29	185.9108	268.44	292.9770
15	523.14	547.6827	161.29	185.8973	318.32	342.8289
50	867.92	892.5364	161.28	185.8855	663.16	687.6878
60	966.82	991.4111	161.30	185.9070	762.00	786.5652
100	1362.58	1387.1865	161.28	185.9089	1157.74	1182.3563
150	1855.62	1880.1951	161.27	185.8140	1650.82	1675.4599
500	5314.41	5339.0649	161.28	185.9018	5109.60	5134.2079
600	6302.16	6326.6993	161.29	185.9044	6097.36	6121.9796
1000	10251.72	10276.3106	161.29	185.8974	10046.90	10071.4583
1500	15191.26	15215.9824	161.29	185.9014	14986.50	15011.1192

Table A.2: Adjusted values of the delay measurement in [ns] if not indicated otherwise.

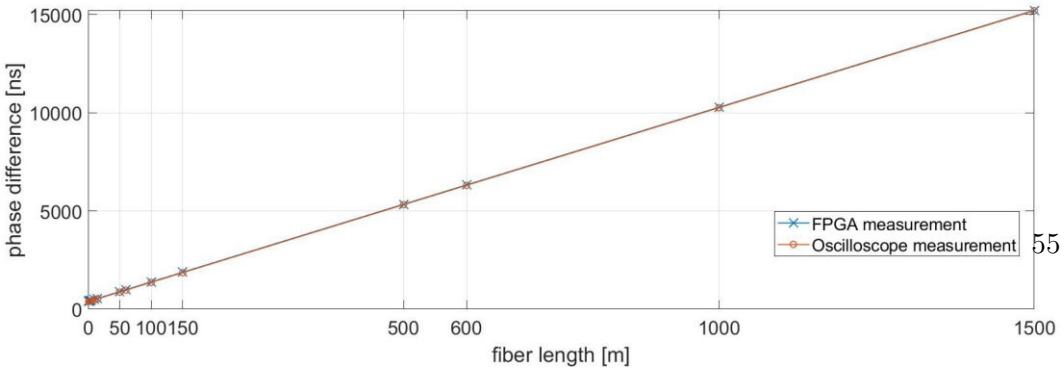

Figure A.34: Normal loopback delay measurement.

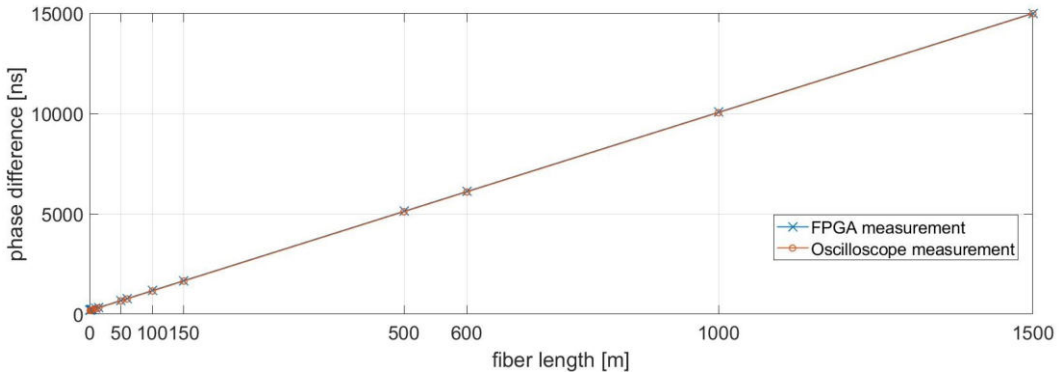

Figure A.35: Remote loopback delay measurement.

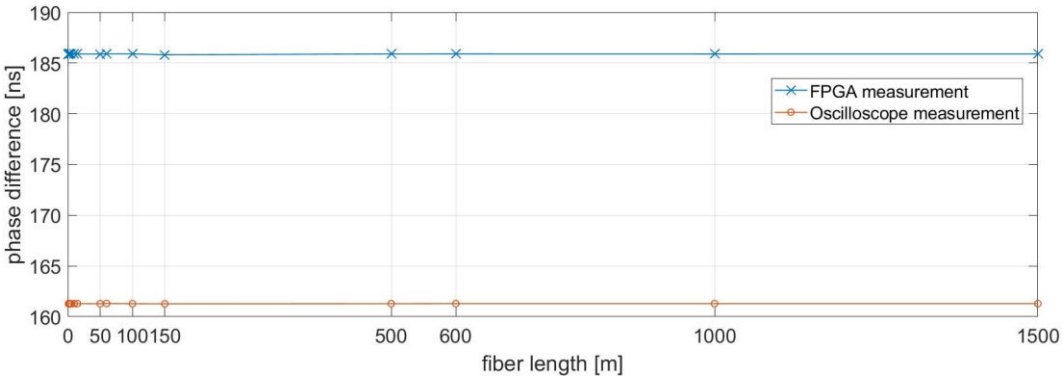

Figure A.36: Local loopback delay measurement.

A.3 Estimation of Uncertainties for the Delay Measurement

The measurement of the loopback delays inherently introduces uncertainties. While the oscilloscope measurement provides uncertainty information directly from the instrument, further analysis is required to determine the sources of uncertainty in the FPGA-based measurement, which involves the following error sources:

1. Uncertainty of the clock frequency: with a clock frequency of $\nu = 125\,\text{MHz}$ the error of 50 ppm translates to $u(\nu) = 6.25\,\text{kHz}$.

2. Jitter in the FPGA: to address this source, $n = 2^{18} = 262144$ measurements

were conducted. The standard deviation calculated from the mean value of the fine time deals with the uncertainty of the jitter.

3. Error in the counting and adaptation process: in the estimation of the coarse time, the counter starts counting one clock cycle later and begins with 0. Consequently, the total delay is 8 ns shorter than it should be. This counting error, along with any potential errors in the adjustment process described in section 3.3, contributes to the general offset between the oscilloscope-based and FPGA measurements.

4. Incorrect fiber lengths: the potential error of the different fiber lengths used does not contribute to the verification of the FPGA-based measurement. Thus, they are not considered for the error estimation of the delay measurements.

The preliminary limiting factor in our measurement is the timing uncertainty in the clock frequency. The periodic time used for estimating both the fine and coarse time through counting is $T = \frac{1}{\nu} = 8\,\text{ns}$. Applying the law of error propagation (as shown in equation A.1)[23], the error for the periodic time is calculated to be $u(T) = 0.0004\,\text{ns}$ (see equation A.2). With increasing fiber length this error gets more significant.

$$u(g) = \sqrt{\sum_{i=0}^{N} \left(\frac{\partial g}{\partial x_i}\right)^2 \cdot u^2(x_i)} \tag{A.1}$$

$$u(T) = \frac{1}{\nu} \cdot u(\nu) \tag{A.2}$$

For each fiber length, the counter saves a different value c. The error for both the fine time and coarse time is $c \cdot u(T)$. In the total error (see equation A.4) the two different counters for both times are referred to as c_{coarse} and c_{fine}.
To address the jitter issue, the standard deviation $u(\overline{x})$ from the mean value $\overline{x}$ for each fine time can be estimated by fitting the histogram with a Gaussian (see equation A.3) [23]. The error resulting from that standard deviation is $u(jitter) = u(\bar{(}x)) \cdot 26.5\,\text{ps}$.

$$a \cdot exp - \frac{(x - \overline{x})^2}{2u(\overline{x}^2} \tag{A.3}$$

Every one of these individual errors contributes to the total error shown in the following equation [23]:

$$u_{total} = \sqrt{u(jitter)^2 + \left(c_{coarse} \cdot u(T)\right)^2 + \left(c_{coarse} \cdot u(T)\right)^2} \tag{A.4}$$

With this equation, the error for each FPGA measurement can be estimated.
For the error bars of figure 3.16 the error of the difference between the oscilloscope and FPGA measurement was calculated with $\sqrt{u(FPGA)^2 + u(oscilloscope)^2}$.

Bibliography

[1] Maurizio Spurio. *Particles and Astrophysics: A Multi-Messenger Approach*. Springer-Verlag GmbH, p. 498. ISBN: 978-3-319-08050-5.

[2] Thomas K. Gaisser, Ralph Engel, Elisa Resconi. *COSMIC RAYS AND PARTICLE PHYSICS*. Cambridge University Press, 2016.

[3] Marica Branchesi. »Multi-messenger astronomy: gravitational waves, neutrinos, photons, and cosmic rays«. In: *Journal of Physics: Conference Series* 718.022004 (2016).

[4] *Baikal-GVD Website*. URL: `https://baikalgvd.jinr.ru/`.

[5] Annarita Margiotta. »The KM3NeT deep-sea neutrino telescope«. In: *Nuclear Instruments and Methods in Physics Research Section A: Accelerators, Spectrometers, Detectors and Associated Equipment* 766 (2014), pp. 83–87.

[6] *KM3NeT Website*. URL: `https://www.km3net.org/`.

[7] *IceCube Neutrino Observatory Website*. URL: `https://icecube.wisc.edu/science/icecube/`.

[8] Elisa Resconi. »The Pacific Ocean Neutrino Experiment«. In: *Proceedings of 37th International Cosmic Ray Conference — PoS(ICRC2021)* (2021).

[9] *P-ONE: Pacific Ocean Neutrino Experiment Website*. URL: `https://www.pacific-neutrino.org/`.

[10] Matthias Danninger Christian Spannfellner. »Pacific Ocean Neutrino Experiment (P-ONE): prototype line development«. In: *Proceedings of Science, 37th International Cosmic Ray Conference (ICRC2021)*. Vol. 395. 2021.

[11] Wolfgang Demtröder. *Experimentalphysik 2 - Elektrizität und Optik*. 7., korrigierte und erweiterte Auflage. 978-3-662-55789-1, 78-3-662-55790-7 (eBook): Springer-Verlag GmbH, 2017, p. 447.

[12] Christopher Fink. »Pacific Ocean Neutrino Experiment: Optical Case Studies for the Multi-PMT Module«. MA thesis. TUPH ECP E49, 2022.

[13] *Elastosil RT 601 A/B - Room Temperature Curing Silicone Rubber (RTV-2)*. Wacker Chemie AG. productinformation@wacker.com, www.wacker.com, 2022.

[14] *Wacker Silgel 612 A/B - Silicone Gels*. Wacker Chemie AG. productinformation@wacker.com, www.wacker.com, 2022.

[15] Marco Winzker Winfried Gehrke. *Digitaltechnik - Grundlagen, VHDL, FPGAs, Mikrocontroller*. 8. Auflage. Springer-Verlag GmbH, p. 701. ISBN: 978-3-662-63953-5, 978-3-662-63954-2 (eBook).

[16] Wolfgang Riggert. *Rechnernetze*. 4., aktualisierte und erweiterte Auflage. München: Carl Hanser Verlag GmbH & amp; Co. KG, 2012. DOI: 10.3139/9783446433861. eprint: https://www.hanser-elibrary.com/doi/pdf/10.3139/9783446433861. URL: https://www.hanser-elibrary.com/doi/abs/10.3139/9783446433861.

[17] *8b/10b encoding*. URL: https://en.wikipedia.org/wiki/8b/10b_encoding.

[18] *TRB Collaboration Website*. URL: http://trb.gsi.de/.

[19] *LatticeECP3 SERDES/PCS Usage Guide - Technical Note*. Lattice Semiconductor Corp. 2020.

[20] URL: https://www.gsi.de/en/researchaccelerators/research_an_overview/hades_experiment.

[21] E. Gousiou et al. J. Serrano M. Cattin. »The White Rabbit Project«. In: *Proceedings of IBIC2013, Oxford, UK* (2013). ISBN 978-3-95450-127-4.

[22] Marc R. Feldman Dustin Tso Sarina Kapai. »D-DMTD: Digital Dual Mixer Timer Difference«. In: (2017).

[23] *Hinweise zur Beurteilung von Messungen, Messergebnissen und Messunsicherheiten (ABW)*. https://www.ph.tum.de/academics/org/labs/ap/org/ABW.pdf. 2020.